Nano Research

ISSN 1998-0124 CN 11-5974/O4
https://doi.org/10.26599/NR.2026.94909292

Research Article

3D-printed flexible piezoelectric scaffolds restore load-bearing function of regenerated bone

Suyun Li[1,§], Yanbo Shan[2,§], Yixuan Wang[1], Zengqin Shi[1], Yifeng Dong[1], Lisheng Zhao[2](✉), Rujie He[1,3](✉), Ying Li[1,3](✉)

[1] Institute of Advanced Structure Technology, Beijing Institute of Technology, Beijing 100081, China

[2] Institute of Stomatology & Oral Maxilla Facial Key Laboratory, First Medical Center of Chinese PLA General Hospital, Beijing 100853, China

[3] Marine Science and Technology Domain, Beijing Institute of Technology, Zhuhai 519088, China

[§] Suyun Li and Yanbo Shan contributed equally to this work.

Nano Res., **Just Accepted Manuscript** • https://doi.org/10.26599/NR.2026.94909292

https://www.sciopen.com/journal/1998-0124 on Oct. 26, 2026

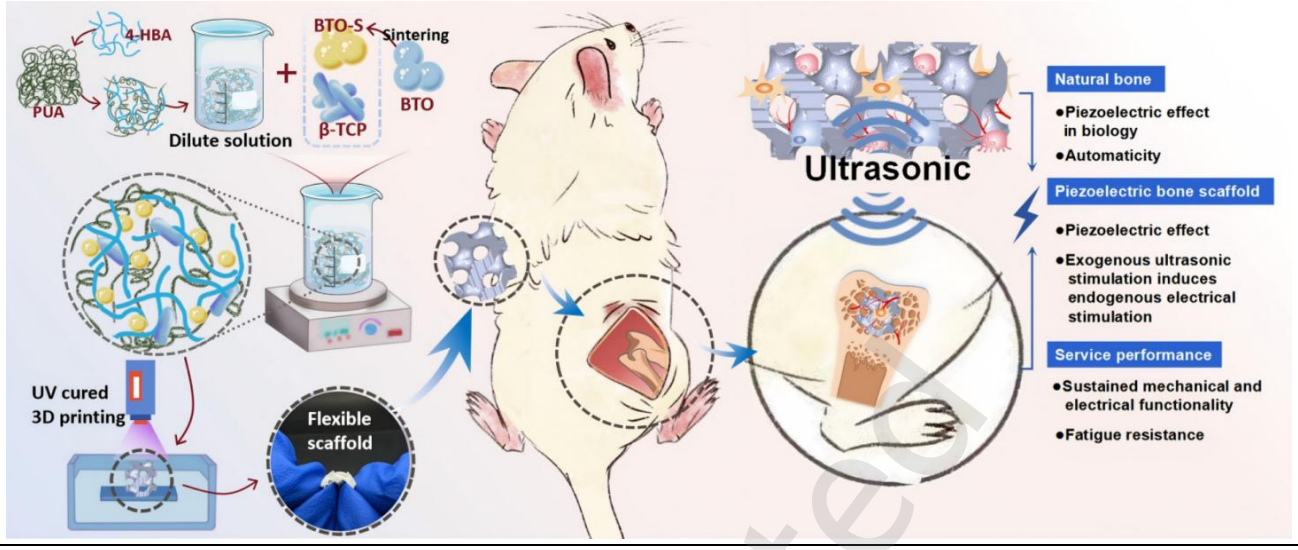
© The Authors(s)

Just Accepted

This is a "Just Accepted" manuscript, which has been examined by the peer-review process and has been accepted for publication. A "Just Accepted" manuscript is published online shortly after its acceptance,which is prior to technical editing and formatting and author proofing. Tsinghua University Press (TUP) provides "Just Accepted" as an optional and free service which allows authors to make their results available to the research community as soon as possible after acceptance. After a manuscript has been technically edited and formatted, and the page proofs have been corrected, it will be removed from the "Just Accepted" web site and published officially with volume and article number (e.g., *Nano Research*, **2025**, *18*, 94906990). Please note that technical editing may introduce minor changes to the manuscript text and/or graphics which may affect the content, and all legal disclaimers that apply to the journal pertain. In no event shall TUP be held responsible for errors or consequences arising from the use of any information contained in these "Just Accepted" manuscripts. To cite this anuscript please use its Digital Object Identifier (DOI®),which is identical for all formats of publication.

Just Accepted

Insert Table of Contents artwork here



PUA/BTO/β-TCP elastomer-ceramic flexible piezoelectric scaffolds were fabricated via DLP 3D printing. Ultrasound excitation significantly promoted bone regeneration in vitro and in a rat femoral defect model, demonstrating that the regenerated bone restored or even surpassed the load-bearing function of the original bone. This led to the proposal of a new paradigm for bone scaffold design, termed "electromechanical adaptation," aimed at long-term in vivo functionality.

Just Accepted

Nano Research

Open Access

Research Article

3D-printed flexible piezoelectric scaffolds restore load-bearing function of regenerated bone

Suyun Li [1,§], Yanbo Shan [2,§], Yixuan Wang [1], Zengqin Shi [1], Yifeng Dong [1], Lisheng Zhao [2]✉, Rujie He [1,3]✉, Ying Li [1,3]✉

[1] *Institute of Advanced Structure Technology, Beijing Institute of Technology, Beijing 100081, China*
[2] *Institute of Stomatology & Oral Maxilla Facial Key Laboratory, First Medical Center of Chinese PLA General Hospital, Beijing 100853, China*
[3] *Marine Science and Technology Domain, Beijing Institute of Technology, Zhuhai 519088, China*
[§] *Suyun Li and Yanbo Shan contributed equally to this work.*

Received: 17 August 2026; **Revised:** 15 October 2026; **Accepted:** 26 October 2026

✉Address correspondence to Lisheng Zhao, zhaolisheng@301hospital.com.cn; Rujie He, herujie@bit.edu.cn; Ying Li, bitliying@bit.edu.cn

Cite this article: *Nano Research*, 2026, 19, 94909292 https://doi.org/10.26599/NR.2026.94909292

ABSTRACT: Flexible piezoelectric scaffolds can conform to irregular bone defects and deliver wireless electrical stimulation, yet whether their mechanical and electrical functions persist throughout the months-long course of bone remodeling, as well as whether the regenerated bone ultimately recovers load-bearing function, remains unresolved. Here, we report PUA/BTO/β-TCP elastomer–ceramic piezoelectric scaffolds fabricated by digital light processing (DLP) into a triply periodic minimal surface (TPMS) architecture. Calcination of BTO increased its ferroelectric tetragonal phase content and enhanced the piezoelectric coefficient d_{33} of the composites by up to 44.3%. The scaffolds combined full elastic recovery after 50% compression with durable mechanoelectrical performance: after 28 days of immersion in simulated body fluid, their quasi-static and cyclic mechanical properties remained essentially unchanged, and d_{33} remained above its initial value. Under ultrasound excitation, the scaffolds significantly enhanced osteoblast proliferation and osteogenic differentiation in vitro and accelerated femoral defect repair in rats, with the bone volume fraction reaching approximately 70% at 8 weeks, versus below 13% for controls. Critically, biomechanical testing at 8 weeks post-implantation showed that the repaired femur withstood a fracture limit load approximately 9.1% higher than that of intact native bone, survived cyclic compression at 70% of the limit load without detectable cracking, and exhibited crack arrest at the scaffold–bone interface, which was direct evidence of stable mechanical integration. We term the concurrent retention of mechanical resilience and piezoelectric output during remodeling, together with stable scaffold–bone mechanical integration, mechanoelectrical adaptation, and propose it as a design principle that shifts bone-scaffold development from short-term osteoinductivity toward sustained in vivo functionality.

KEYWORDS: piezoelectric scaffolds; mechanoelectrical adaptation; elastomer-ceramic composites; load-bearing bone regeneration; long-term in vivo performance

Just Accepted

1 Instruction

Trauma, osteoporosis, and tumor resection frequently result in bone loss [1, 2], producing segmental or localized bone defects of increasing clinical concern [3]. When the defect size exceeds the critical threshold, the limited self-repair capacity of bone becomes insufficient to bridge the defect cavity and achieve healing [4-6]. Implantation of scaffolds with three-dimensional porous architectures is therefore necessary to guide directional tissue ingrowth and enable functional regeneration of critical bone defects [7-10]. Synthetic bone substitutes based on metals and ceramics currently represent primary clinical strategy for bone defect repair [11, 12]; although these materials avoid donor-site complications, they generally suffer from mechanical mismatch with native bone and a lack of osteoinductive activity [13]. Furthermore, traditional research has significantly underestimated the long-term in vivo mechanoelectrical performance of bone scaffolds [14-16].

Natural bone tissue is itself piezoelectric: under mechanical stimulation, it generates endogenous electrical signals that regulate cell proliferation and differentiation [17-19]. To overcome the insufficient biological activity of traditional synthetic bone substitutes [20, 21], piezoelectric bone-tissue-engineering scaffolds have been developed. Piezoelectric ceramics such as barium titanate (BTO) and potassium sodium niobate (KNN) have been incorporated into scaffold designs [22-25], creating biomimetic three-dimensional electrical microenvironments that accelerate bone repair and osseointegration in rat femoral defect models [26]. Coupling additive manufacturing with piezoelectric materials further enables fabrication of ultrasound-responsive scaffolds with customized architectures, achieving wireless, controllable electrical stimulation that promotes neurovascular regeneration in critical cranial defects [27, 28]. These studies demonstrate that reconstructing the electrical microenvironment within the defect site can compensate for the biological deficiencies of traditional materials.

However, rigid piezoelectric ceramics such as BTO [29] suffer from inherent mechanical brittleness and insufficient toughness, rendering them prone to fracture under physiological loads and

difficult to match mechanically with native bone [30]. Their lack of compliance also necessitates surgical incisions considerably larger than the scaffold volume and impedes close conformity to irregular defect geometries [31]. Bone-scaffold design has therefore begun shifting toward "flexibility and mechanoelectrical bioactivity" [32, 33]: integrating elastomer matrices with piezoelectric ceramics yields scaffolds that combine mechanical compliance with osteogenic capacity, paving the way for intraoperative adaptation and precise fitting to complex bone-defect contours [34], as exemplified by the shape-memory piezoelectric Ag-TMSPM-pBT scaffold [35]. Yet a critical question remains unanswered. Bone repair is a dynamic process spanning months to years; throughout cell infiltration, tissue remodeling, and scaffold degradation, stable mechanical support and electrical signal output must be maintained simultaneously. Existing studies focus almost exclusively on electroactive characterization at the initial implantation stage [35], whereas long-term service performance—sustained mechanical and electrical functionality, fatigue resistance, remodeling dynamics, and potential late-stage stress shielding [36, 37]—has rarely been examined. In particular, whether bone regenerated with flexible piezoelectric scaffolds ultimately recovers the load-bearing function of native bone has, to our knowledge, not been established.

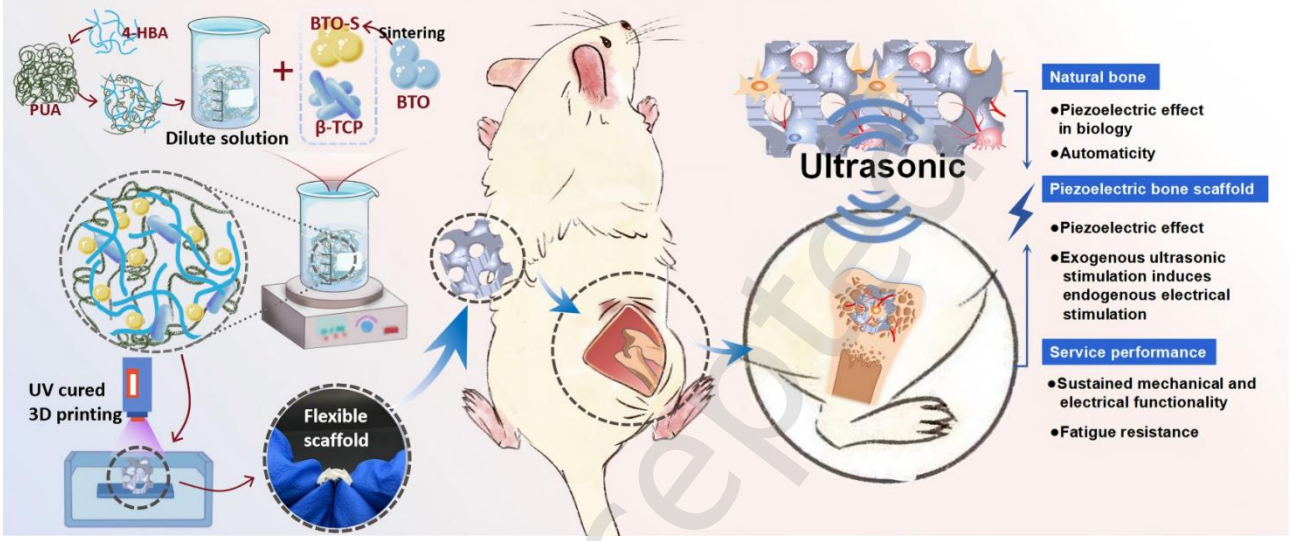


Figure 1. Schematic illustration of 3D-architected PUA/BTO/β-TCP elastomer-ceramic flexible piezoelectric scaffolds for load-bearing bone regeneration.

In this study, we fabricated 3D-architected PUA/BTO/β-TCP elastomer–ceramic flexible piezoelectric scaffolds by DLP-based vat photopolymerization (Figure 1). BTO was calcined to increase its ferroelectric tetragonal phase content, thereby enhancing the piezoelectric response of the resulting composites. Two formulations, 12.5 vol% BTO (denoted P-B12.5T0) and 10 vol% BTO with 2.5 vol% β-TCP (denoted P-B10T2.5), were printed into TPMS architectures with 60% porosity, combining mechanical flexibility and full shape recovery with precise, customizable pore geometries for irregularly shaped defects. We then followed the scaffolds across the full sequence of service conditions: the long-term evolution of their mechanical and piezoelectric properties in simulated body fluid; their in vitro and in vivo osteogenic activity under ultrasound excitation; and, finally, quasi-static and cyclic biomechanical testing of the repaired femurs in direct comparison with intact native bone. Throughout this work, we use the term mechanoelectrical adaptation to denote (i) the concurrent retention of mechanical resilience and piezoelectric output in a physiological environment, (ii) the mechanical conformability of the scaffold to the defect site, and (iii) stable mechanical integration between the implant and host bone during remodeling. Our results show that the repaired femur not only regenerates but recovers and slightly exceeds the load-bearing capacity of native bone, establishing mechanoelectrical adaptation as a practical design principle for the development and clinical translation of load-bearing bone scaffolds.

2 Results and discussion

2.1 Preparation and Characterization of 3D-Printed Flexible Piezoelectric Scaffolds

The maximum ceramic loading supported by the printable elastomer resin matrix was determined experimentally by gradually increasing the solid fraction. When the BTO content reached 12.5 vol%, the slurry viscosity approached the processing limit 3000 mPa·s[38] (Figure S1). To ensure favorable biological characteristics, a TPMS architecture with 60% porosity was selected [39] while maintaining high printing fidelity (Figure S2a-c). Two formulations were chosen for detailed study: 12.5 vol% BTO (P-B12.5T0) and 10 vol% BTO with 2.5 vol% β-TCP (P-B10T2.5). Energy-dispersive spectroscopy confirmed the homogeneous elemental distribution in both composites (Figures S3 and S4).

To enhance piezoelectric response, BTO particles were calcined at 900 °C for 3 h [40]. XRD analysis (Figure 2a) revealed that calcined BTO exhibited a characteristic split peak at 2θ=45°, markedly more pronounced than that of uncalcined BTO, indicating an increased tetragonal phase content. This calcination treatment facilitates the crystallographic transformation from the amorphous/cubic phase to the ferroelectric tetragonal phase with enhanced crystallinity (Figure 2a, c, d). As shown in Figure 2f, the piezoelectric constant d_{33} of calcined P-B12.5T0 reached 2.76 $pC \cdot N^{-1}$, an increase of 24.3% over its uncalcined counterpart, while P-B10T2.5 achieved 2.01 $pC \cdot N^{-1}$, corresponding to a 44.3% enhancement. Hysteresis loop

Just Accepted

measurements (Figure S5) further confirmed the significant improvement in ferroelectric response following calcination.

The mechanical behavior of P-B10T2.5 scaffold with the TPMS architecture was then systematically investigated (Figure 2). Figure 2e illustrates the mechanical performance characteristics of the scaffold. The scaffold is capable of withstanding complex mechanical loads, including compression, bending, and torsion. As the applied load is released, it can fully recover its original shape, avoiding structural failure. This indicates that the P-B10T2.5 scaffold exhibits excellent mechanical stability and perfect shape recovery capability (Figure S6 and S7).

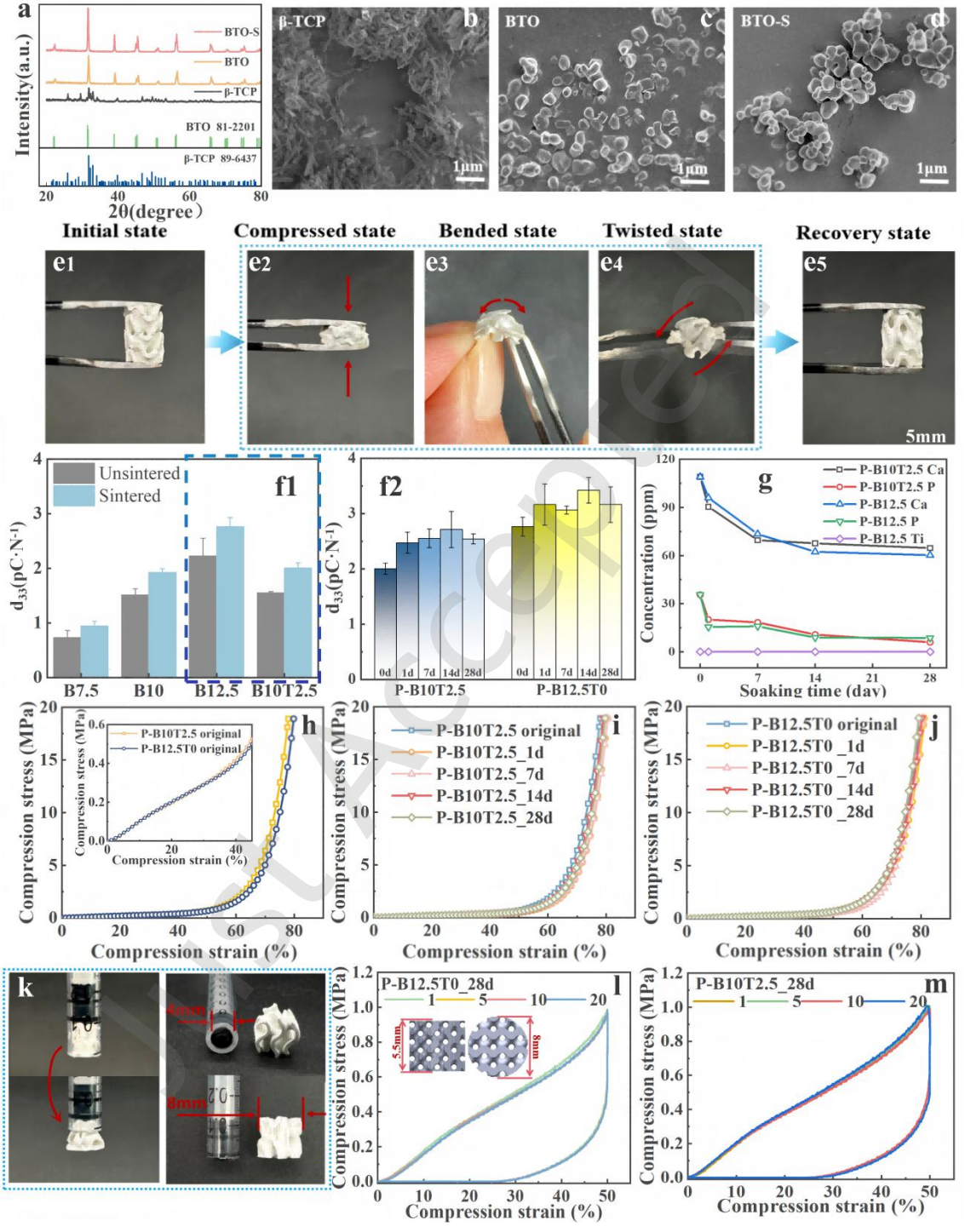


Figure 2. (a) XRD patterns of β-TCP and BTO before and after calcination; (b) microscopic morphology of β-TCP; microscopic morphology of BTO before (c) and after (d) calcination; (e) images of the P-B10T2.5 TPMS scaffold rapidly recovering original shape under various mechanical deformations; (f1) d_{33} of materials with different BTO contents, (f2) variation in d_{33} of P-B10T2.5 and P-B12T0 before and after immersion; (g) ion concentration changes in immersion solutions for P-B10T2.5 and P-B12.5T0 scaffolds; mechanical properties of P-B10T2.5 and P-B12.5T0 before and after SBF immersion: compressive stress-strain curves (h),(i) and (j); (k) demonstration of compressibility of P-B10T2.5 TPMS scaffold; cyclic compressive stress-strain curves of P-B12.5T0 (l) and P-B10T2.5 (m) after 28 days of immersion.

Just Accepted

As shown in Figure 2k, Supplementary Figure S7, and Supplementary Video S1, the PUA/BTO/β-TCP scaffold can be compressed to at least 50% of strain delivered to a target site using a pusher, and then fully recover its shape. This compressibility provides a materials basis for conformable implantation into irregular defects and, potentially, for minimally invasive delivery.

2.2 Long-Term Mechanoelectrical Evolution in a Physiological Environment

The first pillar of mechanoelectrical adaptation is the concurrent retention of mechanical and piezoelectric functionality in a physiological environment. To verify this, simulated body fluid (SBF) immersion experiments were conducted (Figure S8) to comprehensively track the long-term performance evolution of the scaffolds, encompassing piezoelectric and mechanical property retention as well as ion-release behavior, thereby assessing both biological activity and structural integrity.

Quasi-static compressive and tensile properties (Figure 2h, i, j and Figure S6) and cyclic performance (Figure 2l, m and Supplementary Figure S8) were analyzed for scaffolds in their initial state and after immersion for 1, 7, 14, and 28 days. The compression and tension curves of both materials remained largely consistent with their pre-immersion profiles, indicating that the mechanical properties did not deteriorate significantly and demonstrating favorable stability in physiological fluid. Compression stress–strain curves recorded over 20 cycles at 50% strain revealed two characteristic features: (1) a concave profile with an initially steep slope followed by a gradual plateau, indicating a higher elastic modulus at low strain and subsequent stiffness reduction upon entering the yield/densification regime; and (2) the absence of any sharp stress increase up to 50% strain, suggesting that deformation is governed primarily by pore collapse rather than material failure. These results demonstrate the mechanical durability required for long-term in vivo service.

Following SBF immersion, the d_{33} of both scaffolds exhibited an initial increase followed by gradual followed by a gradual decline (Figure 2f2). For P-B10T2.5, the initial d_{33} of 2.01 $pC \cdot N^{-1}$ peaked at 2.71 $pC \cdot N^{-1}$ after 14 days and subsequently settled at 2.54 pC·N-1 at 28 days. Similarly, P-B12.5T0 started at 2.76 $pC \cdot N^{-1}$, peaked at 3.42 $pC \cdot N^{-1}$ after 14 days, and reached 3.16 $pC \cdot N^{-1}$ at 28 days. Notably, in both formulations d_{33} remained above its initial value throughout the 28-day period. This non-monotonic trend reflects the dynamic mechanoelectrical evolution of the scaffolds in a physiological environment: during initial immersion, fluid infiltration and surface mineralization promote charge accumulation at the material–electrolyte interface and thereby enhance the apparent piezoelectric response, whereas with prolonged immersion the progressively thickening mineralized layer facilitates charge leakage, partially degrading the response until equilibrium is established.

Analysis of the immersion solutions (Figure 2g) further revealed rapid initial calcium depletion followed by stabilization. During early immersion (1-7 days), the calcium concentration decreased rapidly, with slightly greater depletion for P-B10T2.5 than for P-B12.5T0, which was consistent with the additional calcium phosphate released from β-TCP. After 7 days, the depletion rate slowed markedly in both groups, eventually stabilizing at approximately 69 ppm, with the equilibrium calcium concentration marginally higher for P-B10T2.5. Phosphorus followed a comparable trend, stabilizing at approximately 11 ppm after 14 days. Titanium content remained negligible (~0 ppm) throughout, attributable to the extremely low solubility of BTO in physiological media—a key factor underlying the retention of piezoelectric properties after 28 days of immersion. Together, these results establish that the scaffolds maintain mechanical resilience and piezoelectric output over a physiologically relevant timescale, fulfilling the first requirement of mechanoelectrical adaptation.

2.3 In Vitro Biocompatibility and Mechanoelectrical Osteogenic Activity

The ultimate success of implantation depends not only on physicochemical properties but also on biological interactions with host tissue. We therefore systematically evaluated the in vitro biocompatibility and mechanoelectrical osteogenic activity of P-B12.5T0 and P-B10T2.5, using a pure PUA scaffold of identical architecture as the Control.

Live/dead staining fluorescence images were quantitatively analyzed (Figures 3a, c). Statistical analysis revealed that ultrasound exposure had no significant effect on cell survival in the Control group, indicating that ultrasound stimulation alone did not substantially promote cell proliferation. In contrast, ultrasound significantly enhanced cell survival in both the P-B10T2.5 and P-B12.5T0 groups: survival rates increased from 96.19% to 96.38% for P-B10T2.5 and from 96.24% to 97.40% for P-B12.5T0. The >1.2% increase in the P-B12.5T0 group suggests a more pronounced responsiveness to ultrasound-induced mechanoelectrical stimulation, consistent with its higher piezoelectric coefficient.

Cell proliferation was assessed by CCK-8 assay after co-culture with MC3T3-E1 cells for 1, 3, and 5 days (Figure 3d). Proliferation increased gradually over time in all groups regardless of ultrasound exposure, indicating the absence of significant cytotoxicity and confirming fundamental biological safety. By day 5, intergroup differences became pronounced: under ultrasound exposure, the P-B10T2.5 group demonstrated significantly higher proliferation than both the Control and P-B12.5T0 groups ($p < 0.001$), indicating superior long-term cell support. Interestingly, despite its lower piezoelectric coefficient, P-B10T2.5 supported higher proliferation under ultrasound—an effect attributable to β-TCP. As a bioactive ceramic, β-TCP gradually releases calcium and phosphate ions, creating a favorable microenvironment for osteoblast adhesion and proliferation; these ions may also modulate intracellular calcium signaling or activate osteogenesis-related gene expression [41].

Alkaline phosphatase (ALP) staining (Figure 3b) revealed only sporadic, faint bluish-purple staining in all groups without ultrasound, indicating basal osteogenic differentiation. Quantitative analysis (Figure 3e) demonstrated that ALP activity in both P-B10T2.5 and P-B12.5T0 was significantly higher under ultrasound exposure ($p < 0.0001$). Under identical ultrasound conditions, ALP activity in the P-B10T2.5 group was significantly higher than in the Control ($p < 0.0001$), while P-B12.5T0 exhibited significantly higher activity than P-B10T2.5 ($p < 0.0001$). This trend contrasts with the CCK-8 results: whereas P-B10T2.5 promoted proliferation through β-TCP-derived ion release, P-B12.5T0—with its higher piezoelectric

In Accepted

output—drove stronger osteogenic differentiation. Together, these findings indicate that bioactive ion release and mechanoelectrical stimulation act on distinct stages of osteoblast behavior through complementary mechanisms.

PCR analysis (Figure 3f-j) revealed no significant differences in osteogenic gene expression in the Control group on day 7 regardless of ultrasound exposure, indicating that neither ultrasound stimulation alone nor the PUA matrix activated osteogenic genes. In contrast, ultrasound significantly upregulated Col-1, OPN, ALP, OCN, and Runx-2 expression in both P-B10T2.5 and P-B12.5T0 ($p < 0.05$), and all gene expression levels were significantly higher in P-B12.5T0 than in P-B10T2.5 ($p < 0.01$). Ultrasound-treated P-B12.5T0 exhibited highly significant upregulation of all detected genes relative to the Control ($p < 0.01$), demonstrating potent mechanoelectrical osteogenic induction. These findings are consistent with the ALP results and collectively establish a quantitative relationship between scaffold piezoelectricity and osteogenic differentiation: external ultrasound converts the piezoelectric phase into an active electrical cue, and the magnitude of the biological response scales with the piezoelectric output of the scaffold. It is noteworthy that the relative advantages of the two scaffolds correspond to different stages of bone repair: P-B10T2.5 excels in cell proliferation (CCK-8), facilitating early cell colonization of the defect, while P-B12.5T0 excels in osteogenic differentiation (ALP, PCR), promoting the maturation of bone tissue; these two abilities shift in importance during the bone healing process (see Section 2.4 for details).

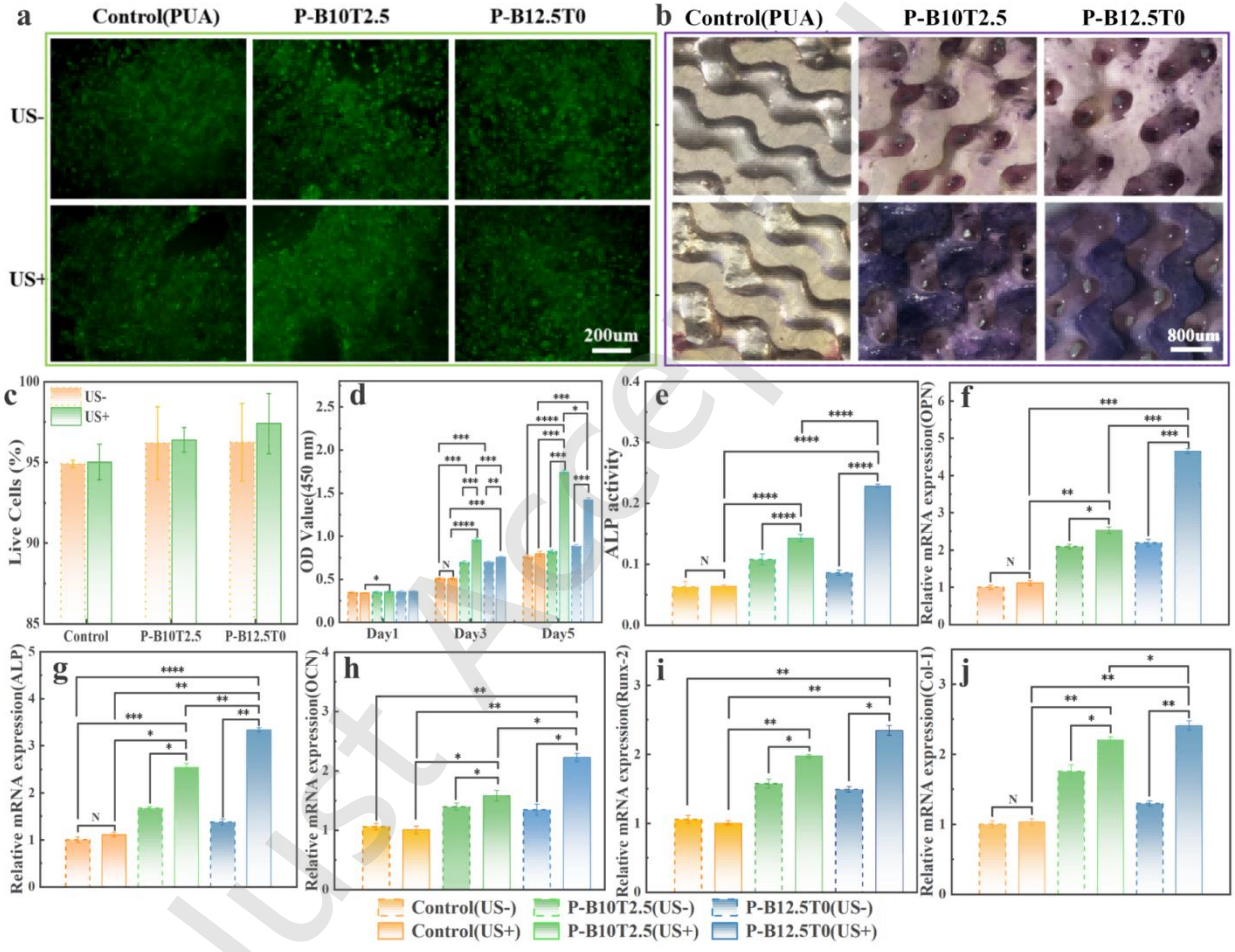


Figure 3. (a) Live/dead staining images and (c) quantitative analysis, (d) CCK-8 proliferation assay of MC3T3-E1 cells cultured with or without ultrasound exposure; (b) ALP staining and (e) quantitative analysis after 7 days of co-culture; relative mRNA expression levels of osteogenic genes (f) OPN, (g) ALP, (h) OCN, (i) RUNX-2, and (j) COL-1 (*$p < 0.05$, **$p < 0.01$, ***$p < 0.001$, ****$p < 0.0001$, $n = 5$).

2.4 In Vivo Mechanoelectrical Bone Regeneration

Cylindrical bone defects (2.5 mm diameter × 3 mm depth) were created in rat femoral condyles using a surgical burr (Figure S9), and femoral samples were harvested at 4 and 8 weeks post-implantation for radiographic and histological analysis. H&E staining of major organs (heart, liver, spleen, lung, and kidney) is presented in Figure 4a. Normal morphological characteristics and cellular architecture were observed across all tissues, with no apparent pathological changes, indicating minimal systemic toxicity and favorable in vivo biocompatibility of the 3D-printed P-B10T2.5 and P-B12.5T0 scaffolds.

Micro-CT-based three-dimensional imaging was performed to assess bone repair in the femoral defect region (Figures 4b-g). Each dataset includes two-dimensional cross-sectional views and spatial distribution reconstructions of new bone based on grayscale-threshold segmentation. Systematic bone morphometric analysis was conducted using quantitative parameters including bone volume fraction (BV/TV, %), trabecular thickness (Tb.Th, mm), trabecular separation (Tb.Sp, mm), bone mineral density (BMD, $mg \cdot cm^{-3}$), trabecular number

(Tb.N, mm^{-1}), and material occupying volume fraction (%). Three-dimensional reconstructed femoral images are provided in Supplementary Figure S10.

At 4 weeks post-implantation (Figure 4b), the Control group exhibited limited new bone formation: regardless of ultrasound stimulation, bone ingrowth remained minimal, with virtually no new bone in the central defect region and nascent bone restricted to the periphery. In contrast, both P-B10T2.5 and P-B12.5T0 demonstrated significantly greater new bone ingrowth, further enhanced under ultrasound exposure. The BV/TV advantage of P-B12.5T0 at 4 weeks is consistent with its high differentiation and gene expression results. Notably, significant new bone formation was observed in the central defect regions under ultrasound stimulation, indicating that mechanoelectrical scaffolds combined with ultrasound promote the progression of bone repair into the defect interior.

By 8 weeks, new bone formation had further increased across all groups. In the P-B10T2.5 and P-B12.5T0 groups, new bone essentially filled the defect space and formed a highly complementary "new bone–implant" composite structure with the porous architecture, indicating inward bone growth along the scaffold pores and favorable three-dimensional osseointegration. Although the Control group exhibited some healing, both the new bone volume and the integrity of its spatial distribution remained significantly inferior. Regarding bone volume fraction (Figure 4d), both experimental groups exhibited significant increases over time. At 4 weeks, the Control BV/TV remained below 7%, whereas both experimental groups exceeded 50% regardless of ultrasound application; specifically, ultrasound-treated P-B10T2.5 achieved 51.04% and P-B12.5T0 reached 55.39% ($p < 0.0001$ vs. Control), with the scaffold material itself occupying approximately 40% of the defect volume. By 8 weeks, the Control BV/TV remained below 13%, whereas ultrasound-exposed P-B10T2.5 and P-B12.5T0 achieved 70.11% and 64.81%, respectively ($p < 0.0001$). Quantitative analysis of trabecular thickness and trabecular separation (Figure 4e and Figure S11) further confirmed that the piezoelectric scaffolds combined with ultrasound continuously promote volumetric repair of the bone defect.

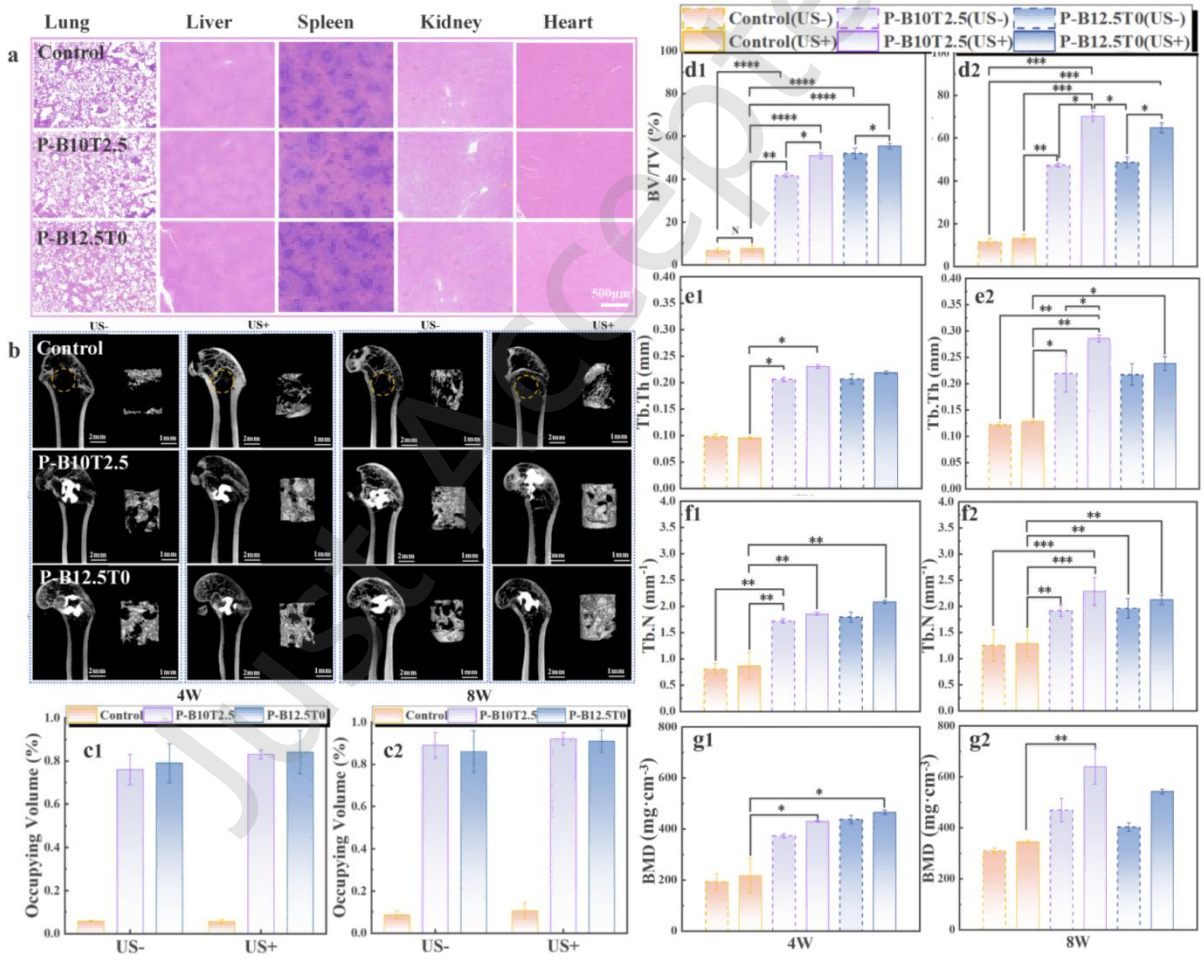


Figure 4. (a) H&E staining of major organs (heart, liver, spleen, lung, kidney) at 4 weeks post-implantation; (b) Micro-CT three-dimensional imaging of femoral defect repair; quantitative analysis of (c) material-occupying volume fraction (%), (d) bone volume fraction (BV/TV, %), (e) trabecular thickness (Tb.Th, mm), (f) trabecular number (Tb.N, mm^{-1}), and (g) bone mineral density (BMD, $mg \cdot cm^{-3}$). (*$p < 0.05$, **$p < 0.01$, ***$p < 0.001$, ****$p < 0.0001$, $n = 5$).

Bone mineral density (BMD) increased in all groups by 8 weeks (Figure 4g). The Control reached 309.55 $mg \cdot cm^{-3}$ without ultrasound and 344.45 mg·cm-3 with ultrasound—substantially lower than the experimental group. P-B10T2.5 under ultrasound achieved 638.9 $mg \cdot cm^{-3}$, significantly exceeding its non-ultrasound counterpart (469.27 $mg \cdot cm^{-3}$, $p < 0.05$); similarly, P-B12.5T0 with ultrasound reached 542.04 $mg \cdot cm^{-3}$, significantly higher than without ultrasound (402.18 $mg \cdot cm^{-3}$, $p < 0.01$).

Notably, the BMD of P-B10T2.5 under ultrasound exceeded that of P-B12.5T0 at 8 weeks—an effect attributable to the continuous release of calcium and phosphate ions from β-TCP, which promotes local mineral deposition. Combined analysis of trabecular number (Tb.N, Figure 4f) and material occupying volume fraction (Figure 4c) revealed that both experimental groups under ultrasound exhibited significantly higher Tb.N than the Control ($p < 0.01$), indicating more compact trabecular structures; concurrently, the material-occupying volume fraction reached 92% and 91% at 8 weeks, confirming substantial defect filling and tight composite formation between the implant and host bone.

Histological analysis provided consistent evidence (Figure 5). H&E staining revealed no inflammatory response or pathological changes in any group. The Control exhibited minimal new bone formation with negligible collagen deposition regardless of ultrasound exposure, whereas both P-B10T2.5 and P-B12.5T0 demonstrated substantially enhanced new bone formation and collagen deposition—particularly under ultrasound stimulation. Masson staining showed that P-B10T2.5 developed numerous mature, tightly arranged bone trabeculae almost completely surrounded by new bone and fibrous tissue, with new bone also evident in the scaffold interior; P-B12.5T0 likewise produced considerable collagen, although the maturity of its bone matrix was slightly lower, with denser new bone at the periphery.

Taken together, the in vivo results reveal a time-dependent complementarity between the two formulations. At 4 weeks, P-B12.5T0, which endowed with higher piezoelectric output, exhibited superior bone regeneration; by 8 weeks, P-B10T2.5 overtook it, with ultrasound further amplifying its osteogenic effect. We attribute this crossover to a two-stage repair mechanism: in the early stage, mechanoelectrical stimulation dominates by reconstructing the electrical microenvironment of the defect and recruiting osteogenic activity; in the later stage, sustained calcium and phosphate ion release from β-TCP increasingly contributes to mineral deposition and trabecular maturation. The piezoelectrically generated electric field may promote cell proliferation and modulate the extracellular microenvironment, and has been reported to induce protein deposition and mineral-ion aggregation on scaffold surfaces, thereby enhancing osteoblast activity—consistent with the quantitative results in Figure 4. This complementarity suggests that piezoelectric output and bioactive ion release can be co-designed to match the temporal sequence of bone healing.

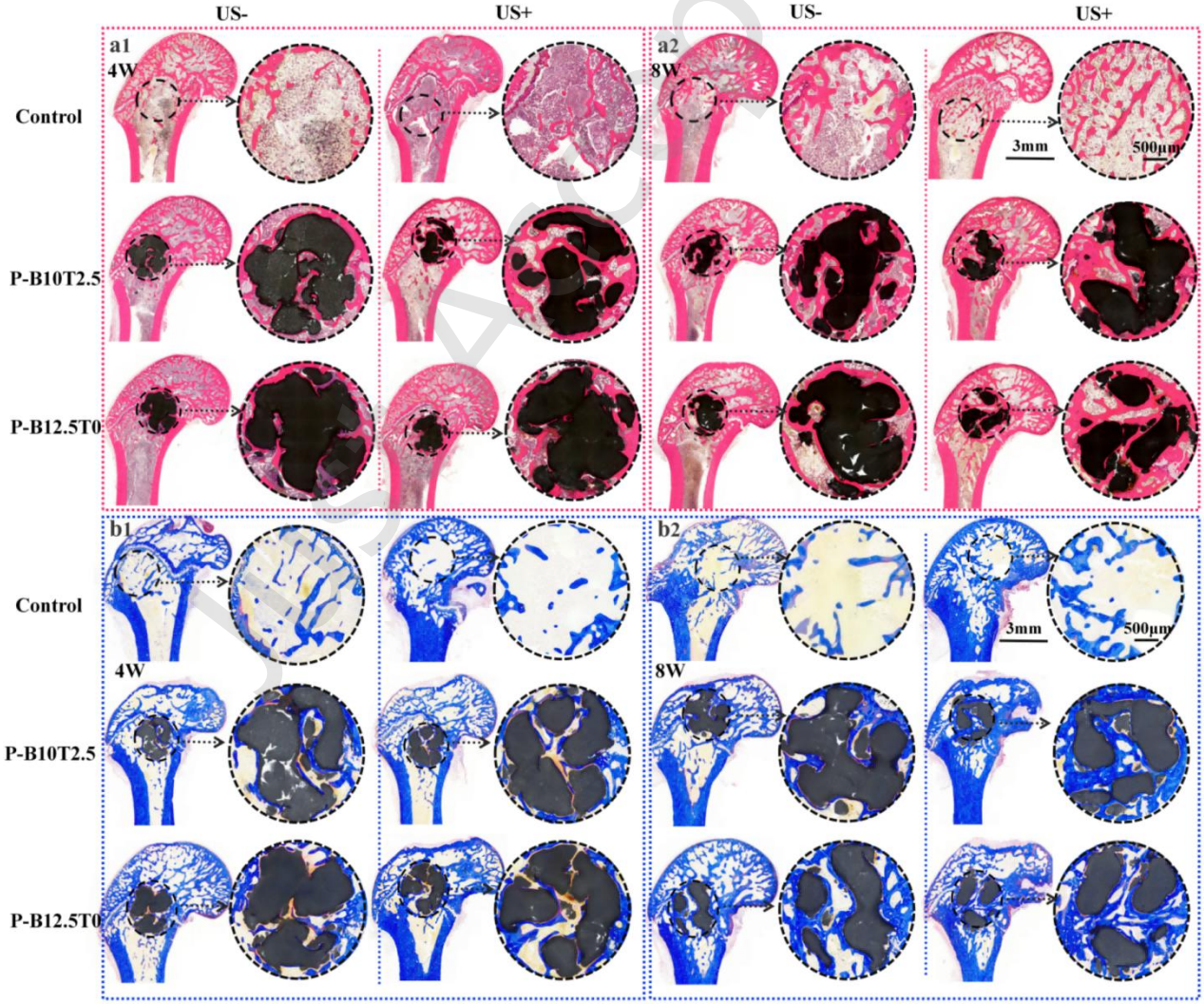


Figure 5. Histological analysis of bone regeneration. (a) H&E and (b) Masson staining images of defect areas in Control, P-B10T2.5, and P-B12.5T0 at 4 and 8 weeks post-implantation.

2.5 Functional Recovery of Load-Bearing Capacity in Repaired Femurs

The preceding sections establish that PUA/BTO/β-TCP scaffolds combine durable mechanoelectrical performance with strong osteogenic activity. The ultimate purpose of a bone scaffold, however, is not merely to fill a defect but to restore the mechanical function of the limb. A critical question therefore remains: can the regenerated bone–implant composite function stably within the complex mechanical environment of the body over the long term? Numerical simulation studies have indicated that when the mechanical properties of callus tissue recover to approximately 70% of those of healthy bone, the stress distribution and deformation of the bone–callus composite under simulated physiological loads closely resemble those of intact bone, with minimal re-fracture risk [42, 43]. Guided by this criterion, we directly compared the biomechanical performance of intact rat femurs with that of femurs repaired with the P-B10T2.5 scaffold at 8 weeks post-implantation.

For the entire rat femur, among feasible in vitro loading modes, axial compression can obtain the most reproducible force-displacement response curve, and using axial compression mode can keep the loading direction consistent with the scaffold defect site. Quasi-static compression testing (n=5) was performed on intact unimplanted rat femurs and on "host bone + P-B10T2.5 implant" composites (denoted Bone-P-B10T2.5) along the orientation shown in Figure 6d. The force–displacement curve of intact femurs comprises three stages: soft-tissue compaction, bone load-bearing, and post-fracture compaction (Figure 6a). The static mechanical response of Bone-P-B10T2.5 followed comparable stages, with an essentially identical slope during the load-bearing phase—indicating that the repaired region transmits load with the same apparent stiffness as native bone. Strikingly, the fracture limit load of Bone-P-B10T2.5 exceeded that of intact bone by approximately 9.1%.

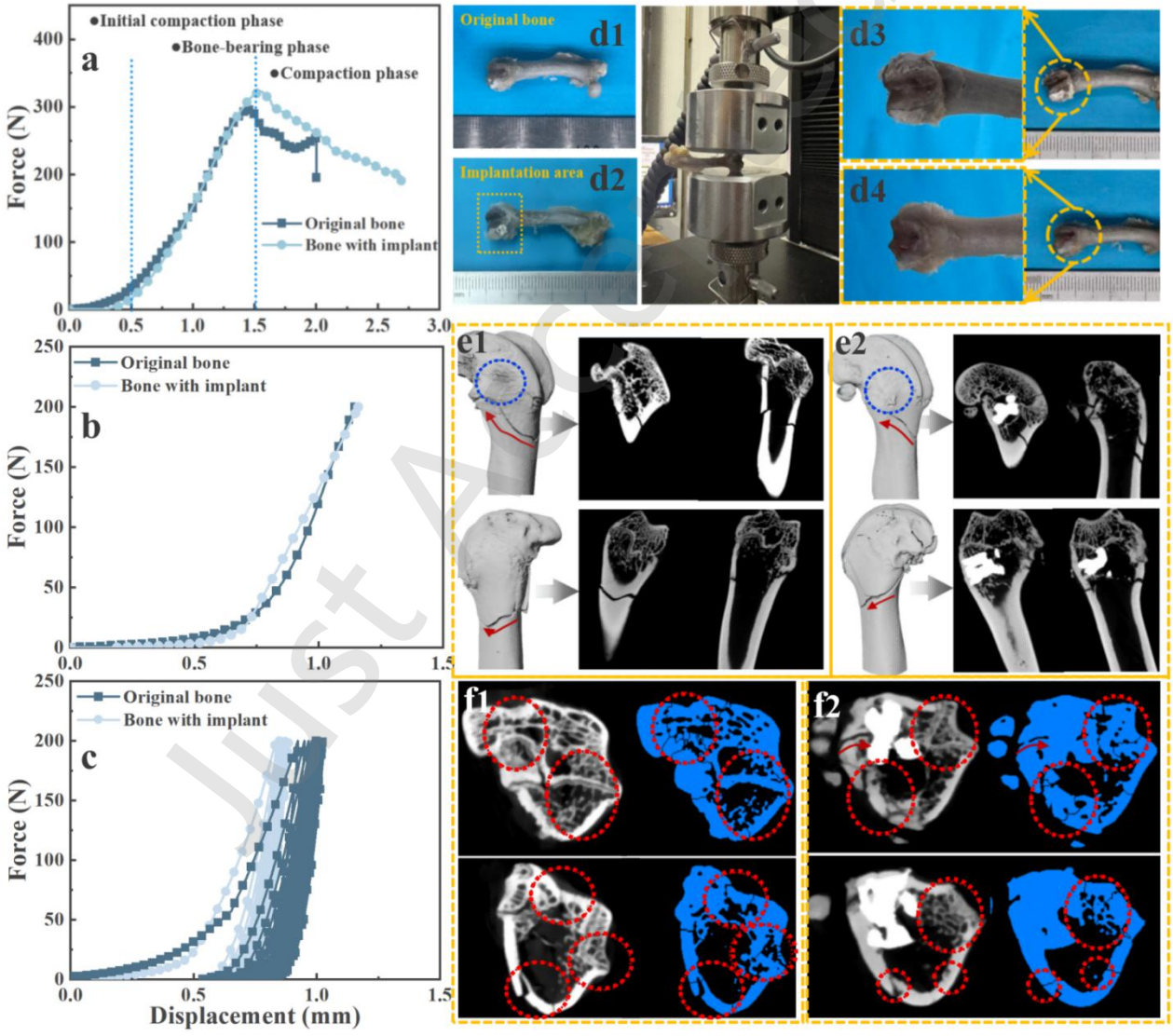


Figure 6. (a) Force–displacement curves of the intact rat femur and the Bone-P-B10T2.5 composite; (b) mechanical response under 70% of the compressive limit load; (c) force–displacement curves of cyclic compression testing at 70% of the limit load (20 cycles); (d) schematic illustration of the axial compression testing configuration and the resulting fracture morphology; (e) 3D CT cross-sectional views of the fracture surfaces; (f) 3D CT reconstruction post-fracture.

Post-fracture analysis revealed the origin of this mechanical competence. Macroscopic observation (Figure 6d) indicated that fracture occurred primarily in the cortical bone region connecting the adductor tubercle and the femoral shaft. Post-fracture CT scans (Figures 6e, f) showed that cracks in intact femurs propagated from cortical to cancellous bone, producing multiple fracture planes. Bone-P-B10T2.5 exhibited consistent macroscopic fracture patterns; however, reconstructed cross-sectional images (Figure 6 f2 and Supplementary Figure S12) demonstrated crack arrest at the scaffold implantation site: the flexible elastomer–ceramic composite remained well integrated with the host bone, without significant interfacial detachment. Rather than acting as a mechanically weak inclusion, the implanted scaffold arrested crack propagation and preserved the integrity of the repaired region—direct evidence of stable mechanical integration between implant and host bone, the third pillar of mechanoelectrical adaptation.

To evaluate functional stability under sustained physiological loading, cyclic compression tests were conducted on Bone-P-B10T2.5 at 70% of the fracture limit load—the threshold identified above as sufficient for near-normal physiological function. No specimen fractured during testing (Figure 6c), and post-cycling Micro-CT reconstructions (Supplementary Figure S13) revealed no significant macro- or micro-cracks; frontal and superior views confirmed intact femoral architecture and interfacial integrity. The elastic modulus of the repaired femur closely approximated that of native bone, indicating no detectable stress-shielding tendency within the testing window. We acknowledge that these measurements were performed ex vivo on whole femurs and thus evaluate the load-bearing function of the repaired femur as an integrated structure rather than replicating any specific in vivo gait cycle. Nevertheless, the convergence of native-level stiffness, a fracture limit load exceeding that of intact bone, interfacial crack arrest, and fatigue resistance under cyclic loading at 70% of the limit load collectively provides strong evidence that the regenerated femur has recovered its load-bearing function.

3. Conclusions

In this study, 3D-architected P-B10T2.5 and P-B12.5T0 elastomer–ceramic piezoelectric scaffolds were fabricated by DLP-based vat photopolymerization 3D printing, with calcination of BTO enhancing the piezoelectric coefficient by up to 44.3%. The scaffolds combined mechanical flexibility with full elastic shape recovery, withstanding complex loading patterns and conforming to complex defect contours—offering a materials basis for conformable and potentially minimally invasive implantation. Long-term immersion in simulated body fluid established the durability of their mechanoelectrical performance: mechanical properties remained essentially unchanged over 28 days, and d_{33} remained above its initial value throughout. In vitro and in vivo experiments under ultrasound excitation demonstrated excellent biocompatibility and osteogenic activity, and revealed a time-dependent complementarity between the two formulations: at 4 weeks, P-B12.5T0 exhibited superior bone regeneration owing to its higher piezoelectric output, whereas by 8 weeks P-B10T2.5 outperformed it, driven by sustained ion release from β-TCP coupled with mechanoelectrical stimulation. Critically, biomechanical analysis of P-B10T2.5-implanted femurs at 8 weeks showed that the repaired bone recovered—and exceeded by approximately 9.1%—the fracture limit load of intact native femur, survived cyclic compression at 70% of the limit load without cracking, and exhibited crack arrest at the scaffold–bone interface, demonstrating stable mechanical integration. These findings establish mechanoelectrical adaptation—the concurrent retention of mechanical resilience and piezoelectric output during remodeling, together with stable scaffold–bone mechanical integration—as a governing design principle for load-bearing bone scaffolds, shifting the design paradigm from short-term osteoinductivity to sustained in vivo functionality. Future work should quantify the electrical output of the scaffolds under ultrasound in vivo and validate long-term load-bearing performance in large-animal weight-bearing models to further advance clinical translation.

4. Experimental Section

4.1 Fabrication of 3D-Printed Elastomer-Ceramic Flexible Piezoelectric Scaffolds

Slurry formulations are detailed in Table S1. UV exposure parameters were optimized for each composition: 27.73 $mW{\cdot}cm^{-2}$ for 10 s VBTO=7.5vol%; 32.74 $mW{\cdot}cm^{-2}$ for 10 s for VBTO=10vol%; 42.55 $mW{\cdot}cm^{-2}$ for 10 s for VBTO=12.5vol%; and 32.74 $mW{\cdot}cm^{-2}$ for 10 s for VBTO/β-TCP=10vol%/2.5vol%. Under a poling electric field of 6 $kV{\cdot}mm^{-1}$ applied for 60 min, the piezoelectric coefficient d_{33} of P-B12.5T0 reached 2.22 $pC{\cdot}N^{-1}$. Further extension of poling time did not enhance the piezoelectric response, whereas increasing the voltage led to dielectric breakdown. For P-B10T2.5, poling at 3.6 $kV{\cdot}mm^{-1}$ for 60 min yield a d_{33} of 1.51 $pC{\cdot}N^{-1}$; exceeding this field resulted in material breakdown.

4.2 Analysis and Characterization

The microstructure of the elastomer–ceramic composite flexible scaffolds was characterized using scanning electron microscopy (SEM, Prisma E, Thermo Fisher Scientific, Czech Republic). Mechanical properties were evaluated using a universal testing machine (Instron 68SC-1, ITW, USA). The piezoelectric strain coefficient d33 was measured using a quasi-static piezoelectric constant tester (ZJ-3A, IACAS, China) following poling. Phase composition was analyzed by X-ray powder diffraction (XRD, Bruker D8 Advance, Bruker, Germany).

4.3 Biological Experiments

Cell viability assay

In vitro cell viability assays were conducted to evaluate the cytocompatibility of the elastomer–ceramic piezoelectric scaffolds. MC3T3-E1 osteoblast (MC3T3-E1, National Collection of Authenticated Cell Cultures, China) were co-cultured with Control, P-B12.5T0, and P-B10T2.5 scaffolds. The culture medium consisted of α-MEM supplemented with 10% fetal bovine serum and 1% penicillin–streptomycin. MC3T3-E1 cells were maintained at 37 °C with 5 vol% CO_2 for subsequent experiments.

MC3T3-E1 cells were seeded at a density of 6×10^3 cells per well onto Control, P-B12.5T0, and P-B10T2.5 scaffolds in two 24-well plates (ultrasound and non-ultrasound groups) and incubated at 37 °C with 5 vol% CO_2 for 72 h. Each group comprised five wells with ultrasound stimulation (US+) and five wells without stimulation (US−). Ultrasound was applied using a UT-1001 device (Baihe Medical Technology, China) at 2.5

Just Accepted

w·cm^{-2} and 1 MHz, twice daily (9:00 and 21:00) for 15 s per session. Following incubation, cells were washed three times with PBS and stained using a Calcein/PI cell viability kit (Calcein: live cells, green; PI: dead cells, red). After 30 min of incubation in the dark, live and dead cells were visualized using a stereomicroscope (SMZ25, Nikon, Japan) with fluorescence channels. Cell counts were quantified using ImageJ software.

CCK-8 proliferation assay

MC3T3-E1 cells were seeded at a density of 6×10^3 cells per well onto Control, P-B12.5T0, and P-B10T2.5 scaffolds in two 24-well plates (ultrasound and non-ultrasound groups) and incubated at 37°C with 5 vol% CO_2 for 24, 72, and 120h, with medium replacement every 72 h. Each group comprised five wells for ultrasound stimulation (US+) and five wells without stimulation (US−). Ultrasound was applied using a UT-1001 device (Baihe Medical Technology, China) at 2.5 w/cm^2 and 1 MHz, twice daily (9:00 and 21:00) for 15 s per session. At 24, 72, and 120 h, the supernatant was carefully aspirated and 100 μL of α-MEM containing 10% CCK-8 solution was added to each well. After 1.5 h incubation, optical density (OD) values were measured at 450 nm using a microplate reader (Epoch 2, USA).

Osteogenic differentiation medium preparation

Osteogenic induction medium was prepared by supplementing basal medium (OriCell, China) with 10% premium fetal bovine serum (OriCell, China) and 1.5% osteogenic induction supplement (OriCell, China) for subsequent MC3T3-E1 osteogenic differentiation experiments.

Alkaline phosphatase staining

MC3T3-E1 cells were seeded at a density of 6×10^3 cells per well onto Control, P-B12.5T0, and P-B10T2.5 scaffolds in two 24-well plate and incubator at 37°C with 5% CO_2 for osteogenic induction. Each group comprised five wells with ultrasound stimulation (US+) and five without (US−). On day 7, samples were washed three times with PBS, fixed with 4% paraformaldehyde at room temperature for 30 min, and washed three times with PBS. ALP staining solution was prepared by adding 10 μL of BCIP solution and 20 μL of NBT solution to 3 mL of ALP colorimetric buffer, mixed thoroughly, and protected from light. Each well received 500 μL of staining solution and was incubated in the dark for 30 min. The staining solution was then aspirated, and the wells were washed three times with PBS. Samples were observed using a stereomicroscope (SMZ25, Nikon, Japan), with three random fields selected per sample for imaging.

Quantitative detection of alkaline phosphatase activity

MC3T3-E1 cells were seeded at a density of 6×10^3 cells per well onto Control, P-B12.5T0, and P-B10T2.5 scaffolds in two 24-well plates and incubator at 37°C with 5% CO_2 for osteogenic induction. Each group comprised five wells with ultrasound stimulation (US+) and five without (US−). On day 7, samples were washed three times with PBS, and 200 μL of cell lysis buffer was added to each well. Cells were thoroughly lysed by repeated pipetting, and the supernatant was collected following centrifugation at 12,000 rpm for 5 min. Protein concentration was determined using a BCA assay kit according to the manufacturer's instructions. ALP activity was measured using an ALP detection kit, with results normalized to ALP expression per unit protein.

Polymerase Chain Reaction (PCR) assay

After 7 days of osteogenic induction, MC3T3-E1 cells co-cultured with Control, P-B12.5T0, and P-B10T2.5 scaffolds were harvested for PCR analysis of osteogenic gene expression. Each group comprised five wells with ultrasound stimulation (US+) and five wells without stimulation (US−). Primer sequences for the osteogenic genes are listed in Table S2.

Total RNA was extracted from each well using the FastPure Cell/Tissue Total RNA Isolation Kit (Vazyme, China) and reverse-transcribed into complementary DNA (cDNA) using 5 × RT Master Mix (TOYOBO, Japan). Real-time PCR was performed using a 2× RealStar Fast SYBR qPCR mixture (Genstar, China) in a StepOne real-time PCR system (Applied Biosystems, China). Gene expression was normalized to GAPDH and analyzed using the $2^{-\Delta\Delta Ct}$ method.

Rat femoral defect model and scaffold implantation

Rats were anesthetized via intraperitoneal injection of 3% sodium pentobarbital (30 mg·kg^{-1}), and the surgical site was disinfected with iodophor. A midline incision was made in the sagittal plane of the right femoral region, with layer-by-layer soft-tissue dissection to expose the femoral condyle. A cylindrical bone defect (2.5 mm diameter × 3 mm depth)[44, 45] was prepared using a surgical drill (Figure S11). The sterilized scaffold was implanted into the defect, and the incision was closed in layers. Postoperatively, general conditions including respiration, activity, and wound healing were monitored daily. Rats were euthanized at 4 and 8 weeks post-implantation, and right femoral specimens were harvested and fixed in 4% paraformaldehyde for subsequent imaging and histological analysis.

Statistical analysis

Experimental data are expressed as mean ± standard deviation (SD), with each experiment conducted independently at least five times ($n \geq 5$). Comparisons between two groups were conducted using an independent-samples t-test, while multiple-group comparisons were performed using one-way ANOVA followed by Tukey's multiple-comparison test. Results are presented as mean ± SEM. Significance is expressed as N (non-significant) or significant (*$p < 0.05$, **$p < 0.01$, ***$p < 0.001$, ****$p < 0.0001$.)

Electronic Supplementary Material: Supplementary material (please provide the brief detail of the ESM) is available in the online version of this article at https://doi.org/10.26599/NR.2026.94909292.

Data availability

All data needed to support the conclusions in the paper are presented in the manuscript and the Electronic Supplementary Material. Additional data related to this paper may be requested from the corresponding author upon request.

Acknowledgements

This work was financially supported by the National Natural Science Foundation of China (Nos.52275310, 52225108).

Declaration of competing interest

All the contributing author(s) report(s) no conflict of interests in

Just Accepted

this work.

Author contribution statement

Suyun Li and Yanbo Shan contributed equally to this work. Rujie He and Ying Li proposed the research concept, Lisheng Zhao and Yifeng Dong suggested the experimental plan. Suyun Li and Yanbo Shan collaboratively completed the scaffold preparation and experimental testing, and analyzed the experimental data. Yixuan Wang and Zengqin Shi were responsible for the mechanical testing experiments. All authors participated in data interpretation, chart organization, and paper writing. Ning Wen, Lisheng Zhao, Rujie He, and Ying Li jointly supervised the entire research project.

Informed consent

Not applicable.

Ethics statement

All the animal experiments were performed with the approval of the Chinese PLA General Hospital Experimental Animal Center, and the animal biomedical research authorization number is 2022-X18-133.

Use of AI statement

None.

References

[1] Zhao, M.; Zhang, X.; Xiao, C.; Chen, X. Biomimetic mineralized hydrogels for bone regeneration. Adv. Mater. 2026, 38, e20380. https://doi.org/10.1002/adma.202520380

[2] Koons, G.L.; Diba, M.; Mikos, A.G. Materials design for bone-tissue engineering. Nat. Rev. Mater. 2020, 5, 584-603. https://doi.org/10.1038/s41578-020-0204-2

[3] Dimitriou, R.; Jones, E.; McGonagle, D. Giannoudis P.V. Bone regeneration: current concepts and future directions. BMC Med. 2011, 9, 66. https://doi.org/10.1186/1741-7015-9-66

[4] Qu, Y.Y.; Shang, Y.F.; Luo, S.X.; Pei, X.M.; Xiao, Y.M.; Zhao, J.M.; Zheng, L.; Liao, C.A.; Liang, R.M. Biodegradable piezoelectric PHB-BT nanofiber scaffolds combined with ultrasound stimulation to accelerate bone regeneration by regulating Ca2+/CaN/NFAT. Theranostics 2026, 16, 4283-4303. https://doi.org/10.7150/thno.124648

[5] Wang, X.J.; Wang, G.W.; Zingales, S.; Zhao, B.D. Biomaterials enabled cell-free strategies for endogenous bone regeneration. Tissue Engineering Part B-Reviews 2018, 24, 463-481. https://doi.org/10.1089/ten.teb.2018.0012

[6] Sawatjui, N.; Damrongrungruang, T.; Leeanansaksiri, W.; Jearanaikoon, P.; Hongeng, S.; Limpaiboon, T. Silk fibroin/gelatin-chondroitin sulfate-hyaluronic acid effectively enhances in vitro chondrogenesis of bone marrow mesenchymal stem cells. Mat. Sci. Eng. C-Mater. 2015, 52, 90-96. https://doi.org/10.1016/j.msec.2015.03.043

[7] Wang, B.; Li, Z.; Jiang, H.; Jiang, Y. Biomaterial-based strategies for neural modulation in innervated bone regeneration. Acta Biomater. 2026, 213, 120-143. https://doi.org/10.1016/j.actbio.2026.02.047

[8] Liu, X.; Wang, Z. Cutting muscle for bone regeneration: striped mineralized muscle with excellent bone repair performance. Chem. Eng. J. 2026, 534, 175134. https://doi.org/10.1016/j.cej.2026.175134

[9] Wang, Y.; Feng, C.; Hou, Z.; Liu, P.; Xu, C.; Chen, X.; Li, Z.; Xiao, Y.; Li, X.; Zhu, X.; Zhang, K.; Mikos, A.G.; Zhang, X. Bone matrix-inspired whitlockite porous ceramic with effects of autophagy activation contributes to bone regeneration. Bioact. Mater. 2026, 61, 657-677. https://doi.org/10.1016/j.bioactmat.2026.02.037

[10] Liang, D.; Wang, H.; Jiang, Y.; Zhang, Z.; Zhou, T.; Ge, S.; Tan, S.; Qin, K.; Wang, Y.; Lin, X.; Xie, Y.; Lyu, H.; Zhang, L. Smart biomaterials for skeletal aging repair and regeneration. Bone Res. 2026, 14. https://doi.org/10.1038/s41413-026-00505-9

[11] Chen, Y.S.; Quan, S.H.; Huang, S.R.; Liu, W.H.; Chen, Z.Y.; Liu, J.H.; Li, C.W.; Yang, H. Applications and progress of 3D printed bioceramic scaffolds in bone tissue repair and immune regulation. Ceram. Int. 2024, 50, 48891-48908. https://doi.org/10.1016/j.ceramint.2024.09.294

[12] Hu, X.Y.; You, D.Q.; Fei, T.Y.; Wu, Y.H.; Shao, Y.J.; Xie, Y.; Xu, M.H.; Hu, Y.J.; Zhang, J.Y.; Yu, M.F. The role and application of metal ions in maxillofacial bone defect. Chem. Eng. J. 2024, 493, 152317. https://doi.org/10.1016/j.cej.2024.152317

[13] Li, L.; Shi, J.; Zhang, K.; Yang, L.; Yu, F.; Zhu, L.; Liang, H.; Wang, X.; Jiang, Q. Early osteointegration evaluation of porous Ti6Al4V scaffolds designed based on triply periodic minimal surface models. J. Orthop. Transl. 2019, 19, 94-105. https://doi.org/10.1016/j.jot.2019.03.003

[14] Yang, S.; Bai, Y.; Shan, Y.; Zhou, Q.; Wang, G.; Zhu, B.; Zhou, Y.; Fang, W.; Wen, N.; He, R.; Zhao, L. 3D-printed strontium-incorporated β-TCP bioceramic triply periodic minimal surface scaffolds with simultaneous high porosity, enhanced strength, and excellent bioactivity. J. Adv. Ceram. 2023, 12, 1671-1684. https://doi.org/10.26599/jac.2023.9220787

[15] Zhang, K.; Zhou, Y. Application of hydroxyapatite nanoparticles in tumor-associated bone segmental defect. Sci. Adv. 2019, 5, eaax6946. https://doi.org/10.1126/sciadv.aax6946

[16] Zhou, J.C.; Georgas, E.; Su, Y.C.; Zhou, J.Y.; Kröger, N.; Benn, F.; Kopp, A.; Qin, Y.X.; Zhu, D.H. Evolution from bioinert to bioresorbable: in vivo comparative study of additively manufactured metal bone scaffolds. Adv. Sci. 2023, 10. https://doi.org/10.1002/advs.202302702

[17] Chorsi, M.T.; Curry, E.J.; Chorsi, H.T.; Das, R.; Baroody, J.; Purohit, P.K.; Ilies, H.; Nguyen, T.D. Piezoelectric biomaterials for sensors and actuators. Adv. Mater. 2019, 31, 1802084. https://doi.org/10.1002/adma.201802084

[18] Yasuda, I.; Fukada, E. On the piezoelectric effect of bone. J. Phys. Soc. Jpn 1957, 12, 10.

[19] Khare, D.; Basu, B.; Dubey, A.K. Electrical stimulation and piezoelectric biomaterials for bone tissue engineering applications. Biomaterials 2020, 258, 120280. https://doi.org/10.1016/j.biomaterials.2020.120280

[20] Xia, D.; Qin, Y.; Guo, H.; Wen, P.; Lin, H.; Voshage, M.; Schleifenbaum, J.H.; Cheng, Y.; Zheng, Y. Additively manufactured pure zinc porous scaffolds for critical-sized bone defects of rabbit femur. Bioac. Mater. 2023, 19, 12-23. https://doi.org/10.1016/j.bioactmat.2022.03.010

[21] Ma, H.; Feng, C.; Chang, J.; Wu, C. 3D-printed bioceramic scaffolds: from bone tissue engineering to tumor therapy. Acta Biomater. 2018, 79, 37-59. https://doi.org/10.1016/j.actbio.2018.08.026

[22] Li, S.; Shan, Y.; Chen, J.; Su, R.; Zhao, L.; He, R.; Li, Y. Piezoelectricity promotes 3D-printed bto/β-tcp composite scaffolds with excellent osteogenic performance. ACS Appl. Bio Mater. 2025, 8, 2204-2214. https://doi.org/10.1021/acsabm.4c01754

[23] Chen, K.; Wang, F.; Sun, X.; Ge, W.; Zhang, M.; Wang, L.; Zheng, H.; Zheng, S.; Tang, H.; Zhou, Z.; Wu, G. 3D-printed zinc oxide nanoparticles modified barium titanate/hydroxyapatite ultrasound-responsive piezoelectric ceramic composite scaffold for treating infected bone defects. Bioact. Mater. 2025, 45, 479-495. https://doi.org/10.1016/j.bioactmat.2024.11.015

[24] Shan, Y.; Xu, L.; et al. A neurodevelopment-inspired self-evolving scaffold for nerve regeneration. Cell Biomater. 2025, 1, 100006. https://doi.org/10.1016/j.celbio.2024.100006

[25] Hua, L.; Ke, Y.; et al. Piezoelectric interfaces pioneering autonomous and personalized diagnostics. MedMat 2025, 2, 145-181. https://doi.org/10.1097/mm9.0000000000000019

[26] Sun, X.; Guo, Y.; Zheng, X.; Bai, Y.; Lu, Y.; Yang, X.; Cai, Z.; Xu, E.; He, Y.; Heng, B.C.; Xu, M.; Deng, X.; Zhang, X. Optimizing the electrical microenvironment provided by 3d micropillar topography on a piezoelectric BaTiO3 substrate to enhance osseointegration. Adv. Mater. 2024, 37, 2414161. https://doi.org/10.1002/adma.202414161

[27] Yang, Y.; Xu, T.; Bei, H.; Zhang, L.; Tang, C.; Zhang, M.; Xu, C.; Bian, L.; Yeung, K.W.; Fuh, J.Y.H.; Zhao, X. Gaussian curvature–driven direction of cell fate toward osteogenesis with triply periodic minimal surface scaffolds. Proc. Natl. Acad. Sci. U.S.A. 2022, 119, e2206684119. https://doi.org/10.1073/pnas.2206684119

[28] Liu, C.; Li, C.; Su, Y.; Ke, Y.; Hao, Z.; Geng, X.; Ge, S.; Yang, Z.; Yang, F.; Ruan, J. Electric - field - assisted 3D printing of personalized piezoelectric implants for non - load - bearing bone fracture repair. Adv. Funct. Mater. 2025, 36, e19617. https://doi.org/10.1002/adfm.202519617

[29] Lei, C.; Lei, J.; Zhang, X.; Wang, H.; He, Y.; Zhang, W.; Tong, B.; Yang, C.; Feng, X. Heterostructured piezocatalytic nanoparticles with enhanced ultrasound response for efficient repair of infectious bone defects. Acta Biomater. 2023, 172, 343-354. https://doi.org/10.1016/j.actbio.2023.10.006

Just Accepted

[30] Zarkoob, H.; Ziaei-Rad, S.; Fathi, M.; Dadkhah, H. An investigation on mechanical behavior of barium titanate foam with hydroxyapatite coating. Ceram. Int. 2012, 38, 3445-3451. https://doi.org/10.1016/j.ceramint.2011.12.057
[31] Chen, J.; Liang, R.; Jia, S. Spatiotemporal adaptation in 4D bioprinting for dynamic bone and cartilage regeneration. Adv. Funct. Mater. 2025, e22357. https://doi.org/10.1002/adfm.202522357
[32] Xu, Y.; Zhang, F.; Zhai, W.; Cheng, S.; Li, J.; Wang, Y. Unraveling of advances in 3D-printed polymer-based bone scaffolds. Polymers 2022, 14, 566. https://doi.org/10.3390/polym14030566
[33] Feng, P.; Wu, P.; Gao, C.; Yang, Y.; Guo, W.; Yang, W.; Shuai, C. A multimaterial scaffold with tunable properties: toward bone tissue repair. Adv. Sci. 2018, 5, 1700817. https://doi.org/10.1002/advs.201700817
[34] Das, R.; Curry, E.J.; Le, T.T.; Awale, G.; Liu, Y.; Li, S.; Contreras, J.; Bednarz, C.; Millender, J.; Xin, X.; Rowe, D.; Emadi, S.; Lo, K.W.H.; Nguyen, T.D. Biodegradable nanofiber bone-tissue scaffold as remotely-controlled and self-powering electrical stimulator. Nano Energy 2020, 76, 105028. https://doi.org/10.1016/j.nanoen.2020.105028
[35] Li, G.; Li, Z.; Min, Y.; Chen, S.; Han, R.; Zhao, Z. 3D‐printed piezoelectric scaffolds with shape memory polymer for bone regeneration. Small 2023, 19, 2302927. https://doi.org/10.1002/smll.202302927
[36] Peidavosi, N.; Azami, M.; Beheshtizadeh, N.; Ramazani, S.A. Piezoelectric conductive electrospun nanocomposite pcl/polyaniline/barium titanate scaffold for tissue engineering applications. Sci. Rep-UK 2022, 12, 20828. https://doi.org/10.1038/s41598-022-25332-w
[37] Zhang, L.; Yang, G.; Johnson, B.N.; Jia, X. Three-dimensional (3D) printed scaffold and material selection for bone repair. Acta Biomater. 2019, 84, 16-33. https://doi.org/10.1016/j.actbio.2018.11.039
[38] Griffith, M.L.; Halloran, J.W.; Freeform fabrication of ceramics via stereolithography, J. Am. Ceram. Soc. 1996, 79, 2601-2608. https://doi.org/10.1111/j.1151-2916.1996.tb09022.x.
[39] Shen, M.; Li, Y.; Lu, F.; Gou, Y.; Zhong, C.; He, S.; Zhao, C.; Yang, G.; Zhang, L.; Yang, X.; Gou, Z.; Xu, S. Bioceramic scaffolds with triply periodic minimal surface architectures guide early-stage bone regeneration. Bioact. Mater. 2023, 25, 374-386. https://doi.org/10.1016/j.bioactmat.2023.02.012
[40] Roy, S.C.; Bhatnagar, M.C.; Sharma, G.L.; Manchanda, R.; Balakrishnan, V.R. Effect of Pre-Sintering Temperature on the Structural and Dielectric Properties of (Ba0.5Sr0.5)TiO3 thin films deposited by sol-gel technique. Ceram. Int. 2004, 30, 2283-2287. https://doi.org/10.1016/j.ceramint.2004.01.008
[41] Heng, B.C.; Bai, Y.; Li, X.; Lim, L.W.; Li, W.; Ge, Z.; Zhang, X.; Deng, X. Electroactive biomaterials for facilitating bone defect repair under pathological conditions. Adv. Sci. 2022, 10, 2204502. https://doi.org/10.1002/advs.202204502
[42] Singh Gangwar, A.K.; Sudhakar Rao, P. Kumar, A. Bio-mechanical design and analysis of femur bone. Materials Today: Proceedings 2021, 44, 2179-2187. https://doi.org/10.1016/j.matpr.2020.12.282
[43] Claes, L.; Augat, P.; Suger, G. Wilke, H.J. Influence of size and stability of the osteotomy gap on the success of fracture healing. J. Orthop. Res. 2005, 15, 577-584. https://doi.org/10.1002/jor.1100150414
[44] Kang, F.; Yi, Q.; Gu, P.; et al. Controlled growth factor delivery system with osteogenic-angiogenic coupling effect for bone regeneration. J Orthop Translat. 2021;31:110-125. https://doi.org/10.1016/j.jot.2021.11.004.
[45] Li, J.; Deng, C.; Liang, W.; et al. Mn-containing bioceramics inhibit osteoclastogenesis and promote osteoporotic bone regeneration via scavenging ROS. Bioact Mater. 2021;6:3839-3850. https://doi.org/10.1016/j.bioactmat.2021.03.039.

© The Author(s) 2026. *Nano Research* published by Tsinghua University Press. The articles published in this open access journal are distributed under the terms of the Creative Commons Attribution 4.0 International License (http://creativecommons.org/licenses/by/4.0/), which permits use, distribution and reproduction in any medium, provided the original work is properly cited.

Just Accepted

Electronic Supplementary Material

3D-printed flexible piezoelectric scaffolds restore load-bearing function of regenerated bone

Suyun Li [1,§], Yanbo Shan [2,§], Yixuan Wang [1], Zengqin Shi [1], Yifeng Dong [1], Lisheng Zhao [2]✉, Rujie He [1,3]✉, Ying Li [1,3]✉

[1] *Institute of Advanced Structure Technology, Beijing Institute of Technology, Beijing 100081, China*
[2] *Institute of Stomatology & Oral Maxilla Facial Key Laboratory, First Medical Center of Chinese PLA General Hospital, Beijing 100853, China*
[3] *Marine Science and Technology Domain, Beijing Institute of Technology, Zhuhai 519088, China*
[§] *Suyun Li and Yanbo Shan contributed equally to this work.*

✉Address correspondence to Lisheng Zhao, zhaolisheng@301hospital.com.cn; Rujie He, herujie@bit.edu.cn; Ying Li, bitliying@bit.edu.cn

Supporting information to https://doi.org/10.26599/NR.2026.94909292

Table S1 DLP 3D printing slurries ratio

Designation	Solid material and its content (vol.%)	Resin matrix content (vol.%)		
		PUA(49wt%)	4-HBA(49wt%)	TPO-L（2wt%）
P-B7.5T0	7.5 BTO	92.5		
P-B10T0	10 BTO	90		
P-B12.5T0	12.5 BTO	87.5		
P-B10T2.5	BTO10/β-TCP2.5	87.5		

Table S2 Primer sequences used in rPCR

Genes	Primer sequences
Col-1	Forward – GGGACCAGGAGGACCAGGAAGT Reverse – GGAGGGCGAGTGCTGTGCTTT
OPN	Forward – AGCAAGAAACTCTTCCAAGCAA Reverse – GTGAGATTCGTCAGATTCATCCG
OCN	Forward – CCAAGCAGGAGGGCAATA Reverse – TCGTCACAAGCAGGGTCA
ALP	Forward – ATCTTTGGTCTGGCTCCCATG Reverse – TTTCCCGTTCACCGTCCAC
Runx-2	Forward – GAACCAAGAAGGCACAGACAA Reverse – GGCGGGACACCTACTCTCATAC
GAPDH	Forward – GTATTGGGCGCCTGGTCACC Reverse – CGCTCCTGGAAGATGGTGATGG

Just Accepted

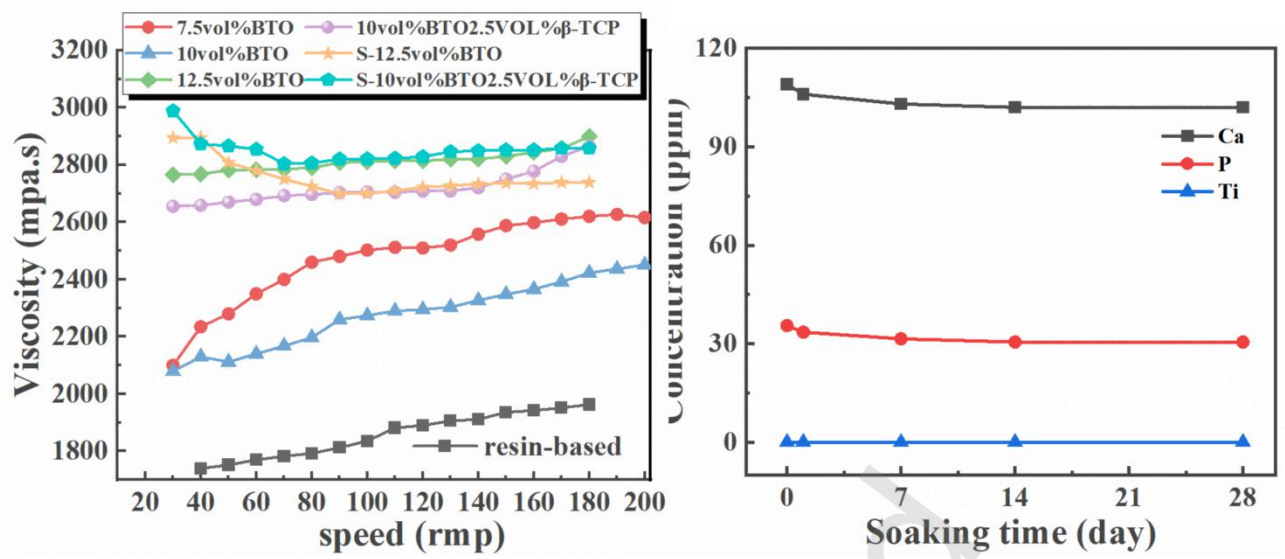


Figure S1 Viscosity curves of slurries with different solid contents, and ion concentration curves after soaking in SBF solution for 28 days

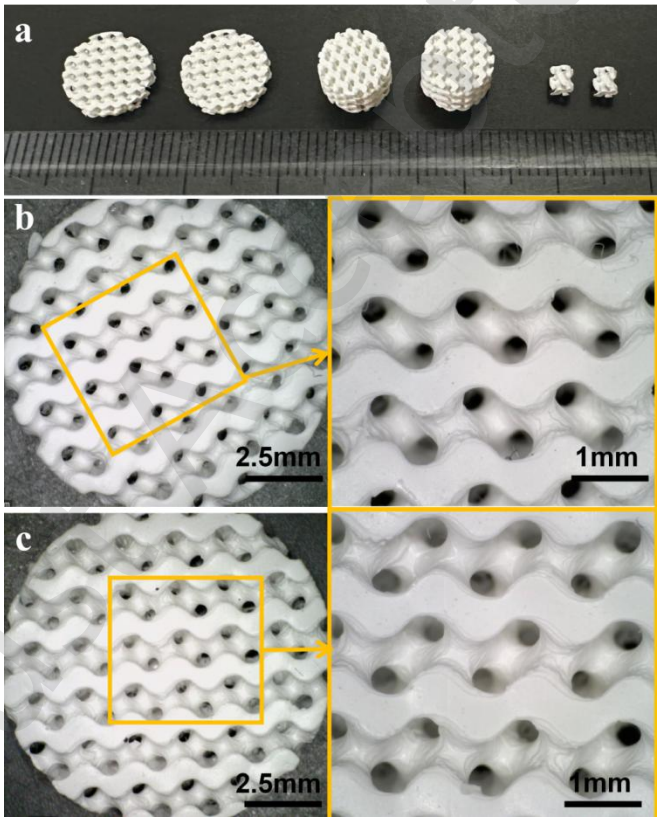


Figure S2 Morphology diagram of P-B12.5T0 and P-B10T2.5 flexible piezoelectric scaffolds. (a) Photographs of P-B12.5T0 and P-B10T2.5 flexible piezoelectric scaffolds for in vitro cell experiments, mechanical testing, and in vivo implantation; (b) detailed view of P-B12.5T0 scaffold for in vitro cell experiments; (c) detailed view of P-B10T2.5 scaffold for in vitro cell experiments.

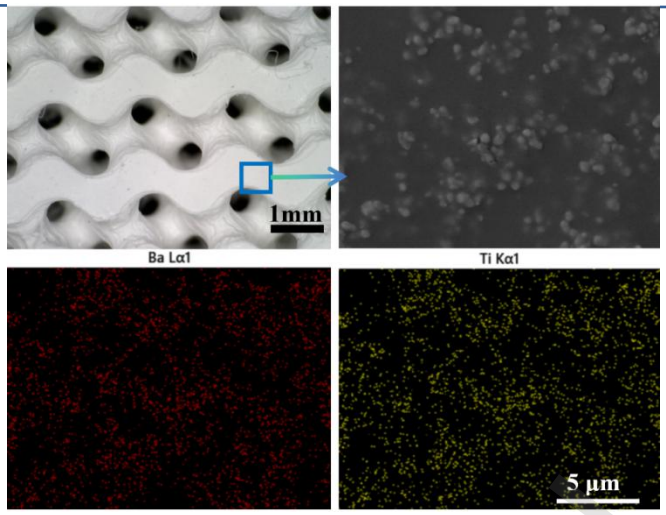


Figure S3 EDS spectrum of P-B12.5T0 scaffold.

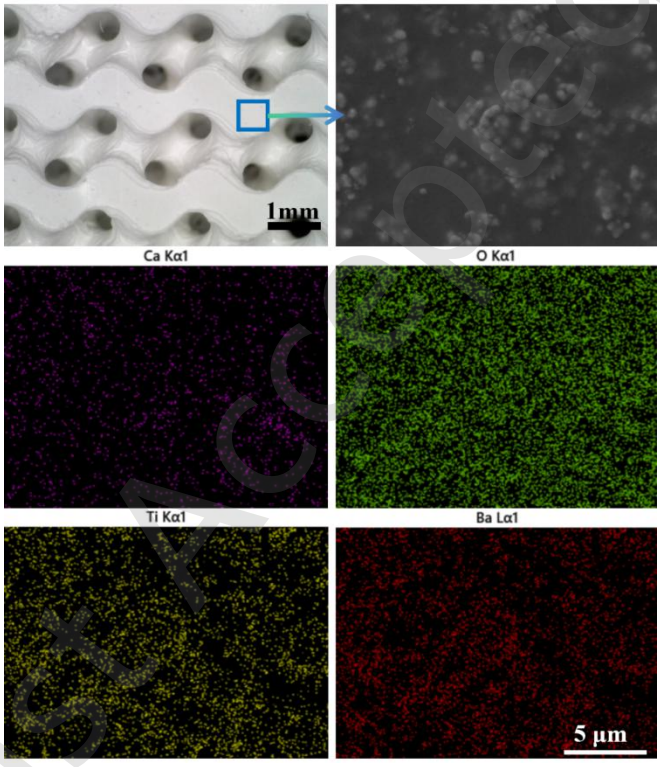


Figure S4 EDS spectrum of P-B10T2.5 scaffold.

Just Accepted

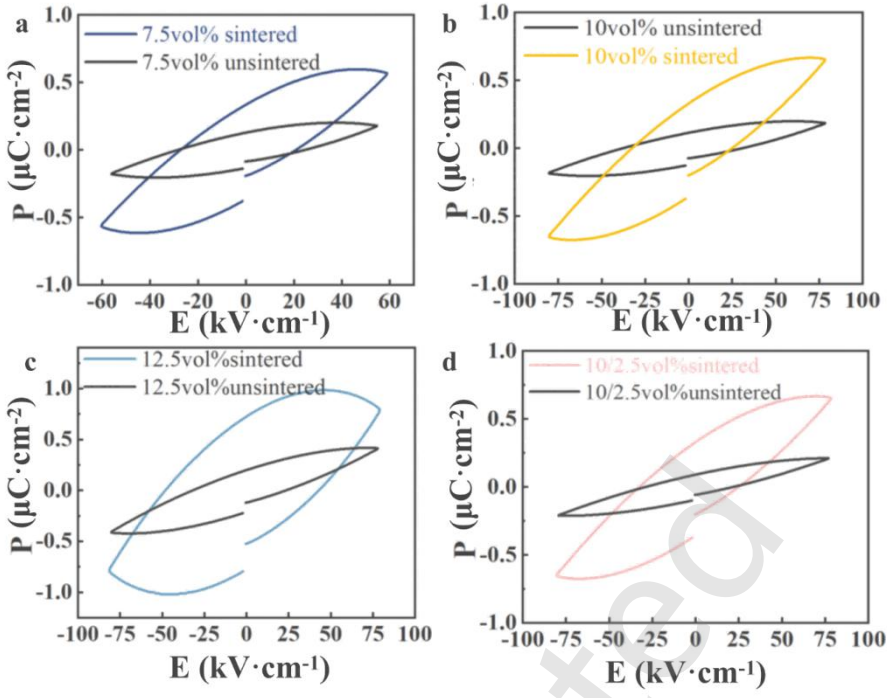


Figure S5 P-E hysteresis loops of flexible piezoelectric composites with pre-sintered and un-sintered BTO at various solid contents.

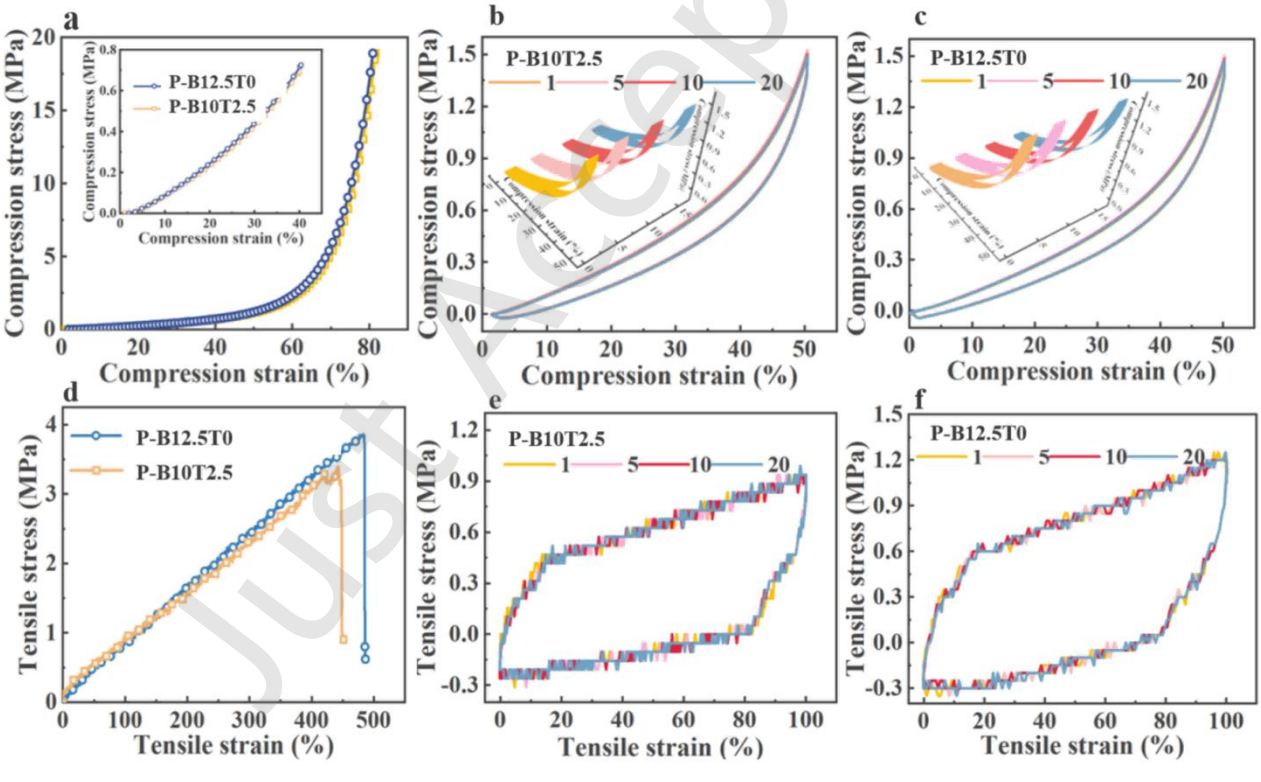


Figure S6 Mechanical properties of P-B12.5T0 and P-B10T2.5 flexible composites (tensile rate: 500 mm·min^{-1}, compression rate: 1 mm·min^{-1}, n = 5). (a) Compressive stress-strain curves; (b) 20-cycle compression of P-B10T2.5; (c) 20-cycle compression of P-B12.5T0; (d) tensile stress-strain curves; (e) 20-cycle tension of P-B10T2.5; (f) 20-cycle tension of P-B12.5T0.

Just Accepted

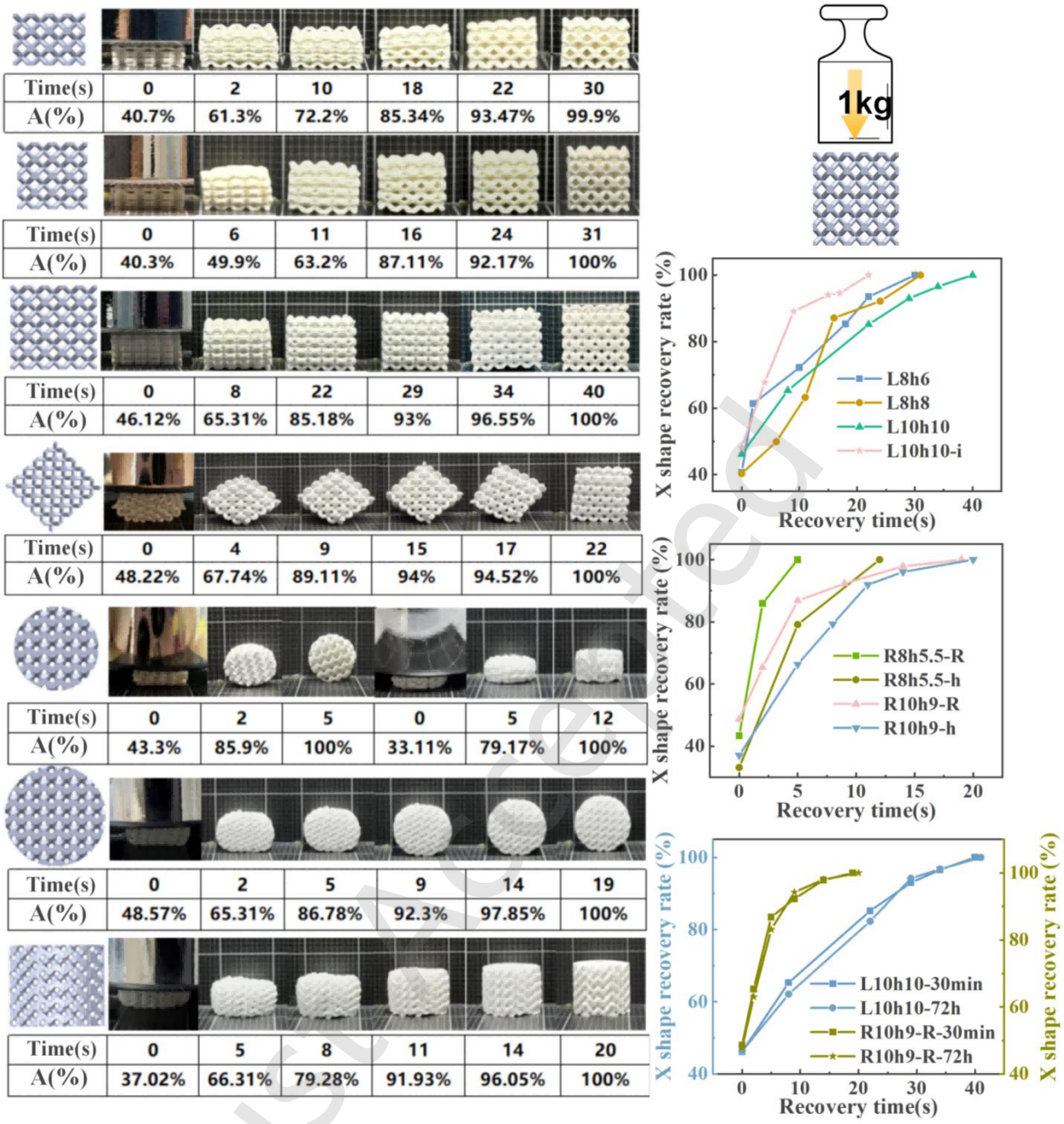


Figure S7 Compression and recovery behavior of P-B10T2.5 scaffolds with different architectures.

Just Accepted

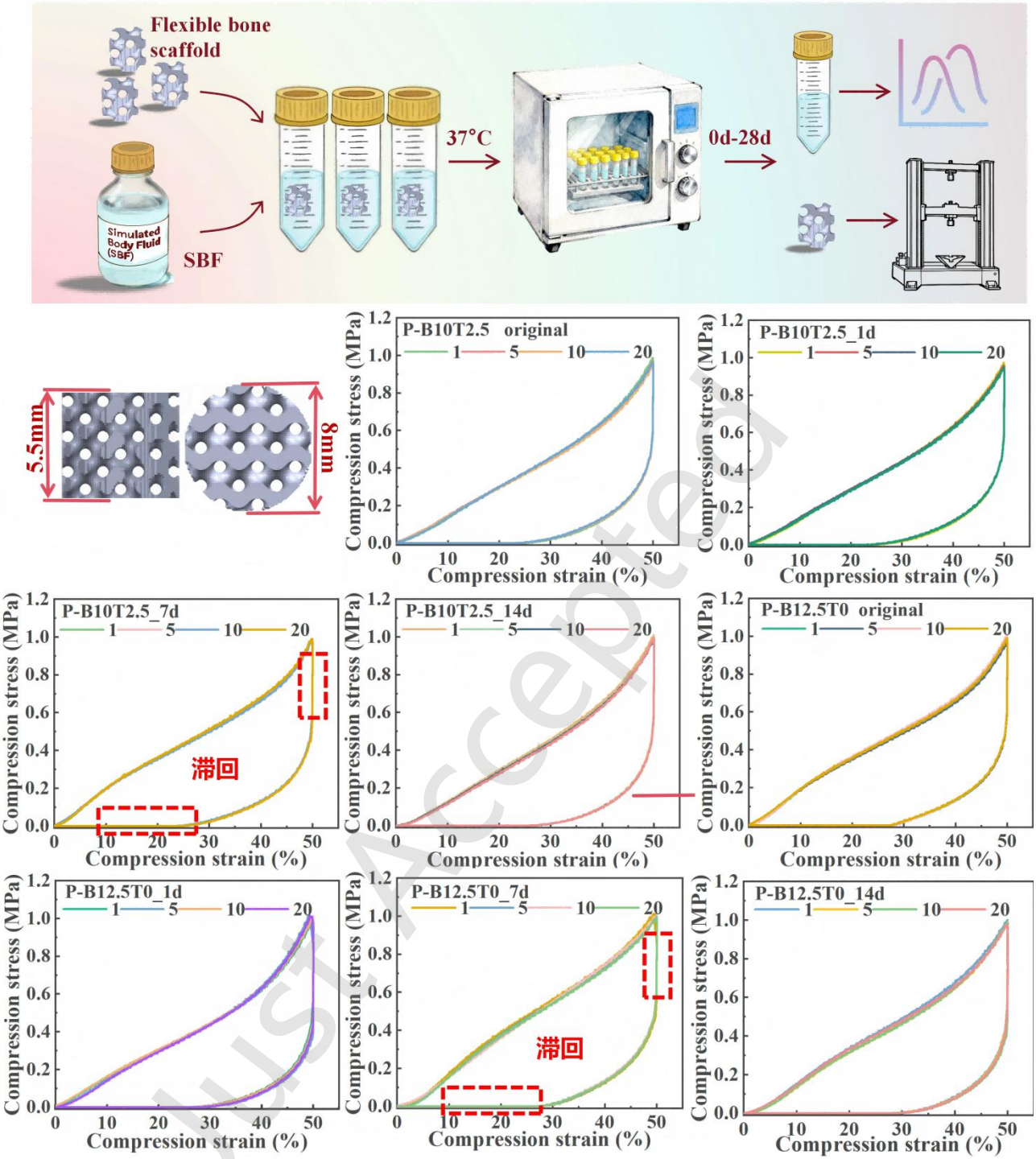


Figure S8 Cyclic mechanical properties of P-B10T2.5 before and after immersion for 1, 7, and 14 days.



Figure S9 Surgical schematic of rat femoral defect model.

Just Accepted



Figure S10 Micro-CT 3D reconstructions of P-B10T2.5 and P-B12.5T0 flexible piezoelectric bone implants at 4 and 8 weeks post-implantation.

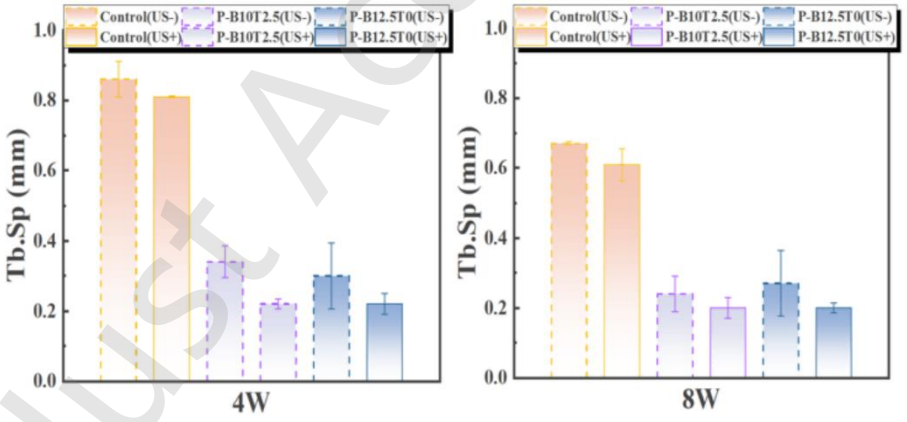


Figure S11 Quantitative analysis of trabecular separation (Tb.Sp, mm) based on Micro-CT 3D imaging results.

Just Accepted

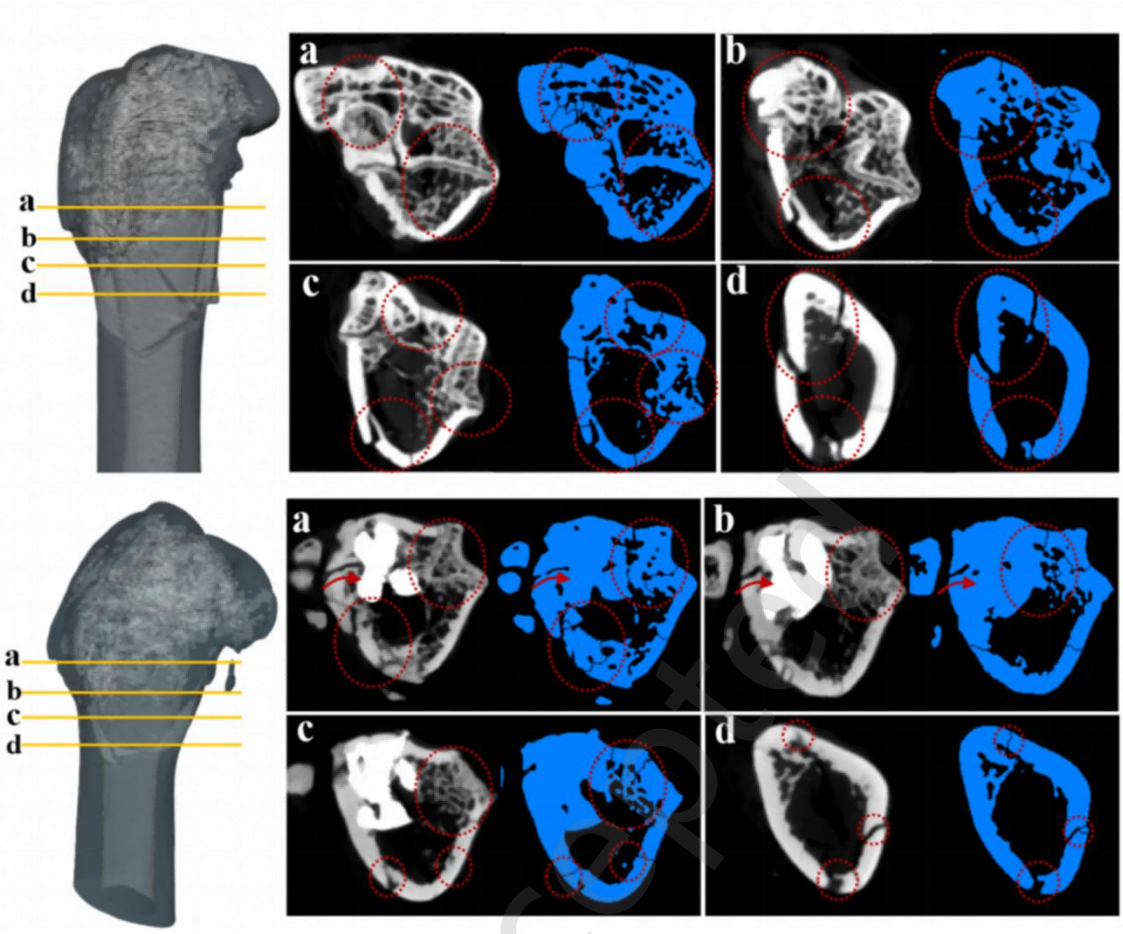


Figure S12 3D CT reconstruction of intact femur and P-B10T2.5-implanted femur at 8 weeks post-implantation following quasi-static compression failure testing.

Just Accepted

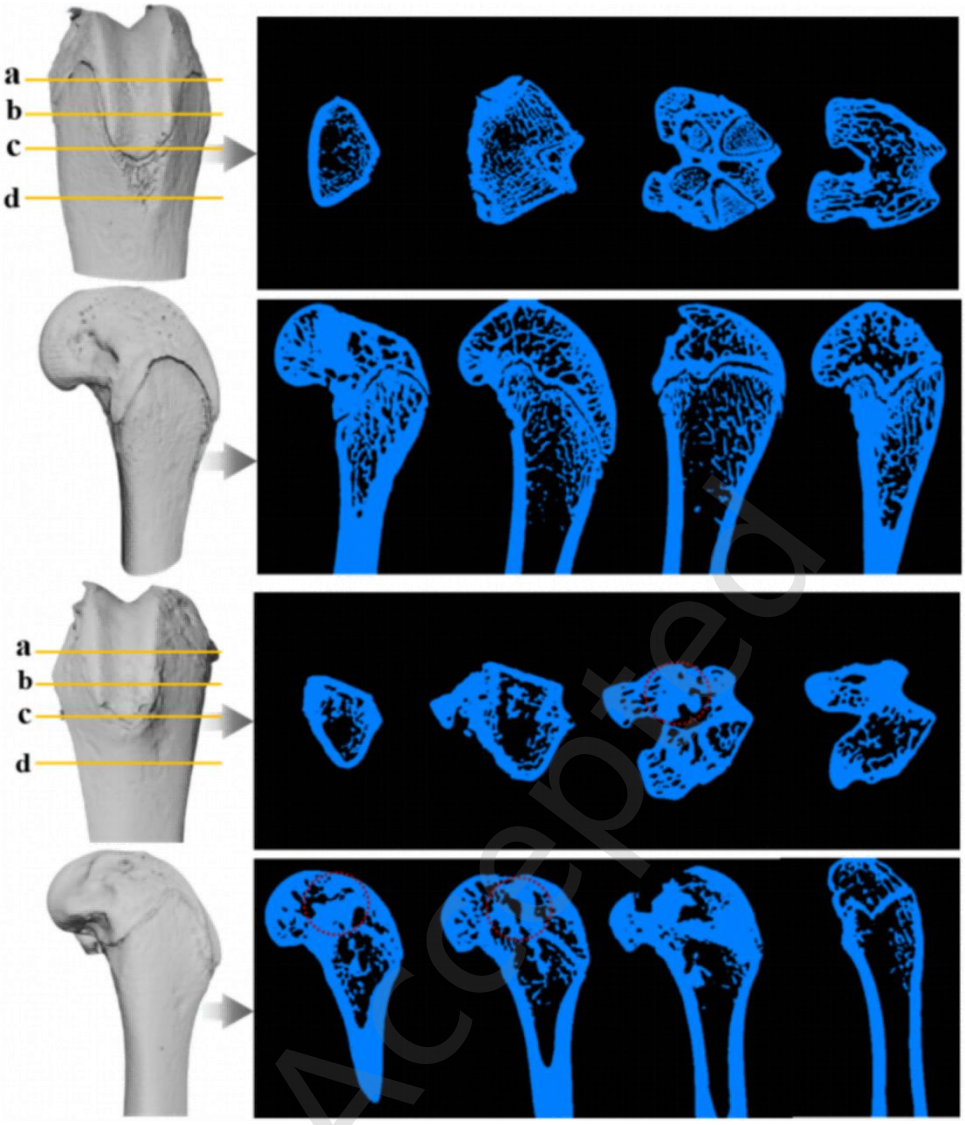


Figure S13 3D CT reconstruction of intact femur and P-B10T2.5-implanted femur after 8 weeks of cyclic compression testing at 70% of limit load.

Just Accepted